# CPO and quantitative textural analyses within sheath folds

E. Fazio [a,*], G.I. Alsop [b], L. Nania [c], R. Graziani [c], S. Iaccarino [d], C. Montomoli [d], R. Carosi [d],
V. Luzin [e], F. Salvemini [e], S. Gambino [a], R. Cirrincione [a], M.A. Mamtani [f]

[a] *Dipartimento di Scienze Biologiche Geologiche e Ambientali, Università di Catania, Italy*
[b] *School of Geosciences, University of Aberdeen, Aberdeen, AB24 3UE, UK*
[c] *Geological Survey of Canada, Natural Resources Canada, Ottawa, Canada*
[d] *Dipartimento di Scienze Della Terra, Università di Torino, Italy*
[e] *Australian Nuclear Science and Technology Organization (ANSTO), Lucas Heights, NSW, Australia*
[f] *Department of Geology & Geophysics, Indian Institute of Technology, Kharagpur-721302, West Bengal, India*

ARTICLE INFO

ABSTRACT

We investigate the intra- and inter-crystalline deformation processes involved in sheath fold development combining complementary fabric analysis techniques and 3D modelling by neutron tomography. The investigated sheath fold is a multi-layered sub-metre scale single-eye structure, developed in metapsammites from the Ben Hope Nappe, overlying the Moine Thrust Zone of NW Scotland. Crystallographic Preferred Orientations (CPOs) of quartz and biotite were acquired through a Neutron Diffractometer and an SEM-EBSD system to compare the full-fabric of the main phases and the active slip systems for an "in situ" structural control. Combined with orientation maps and grain size maps, results show that, despite the different structural positions of the investigated microdomains (upper vs lower fold limbs, inner vs outer sheath closures, distance from hinge of the sheath fold), quartz and biotite deformed uniformly, suggesting a constant differential stress and orientation of the kinematic vorticity axis. Previously recognized detachment horizons within the sampled sheath fold do not affect the fabric patterns recorded by quartz and biotite. This may be interpreted in two different ways: i) detachments formed during earlier active folding and prior to passive amplification of folds associated with more uniform flow to create the sheath fold geometries; ii) the quartz c-axis patterns are coeval with a late deformation phase (loading of the orogenic wedge) that pervasively obliterated the previous fabric and therefore did not preserve the active folding component. Several pieces of evidence reported here, such as top-to-SE normal-shear sense which is opposite to the regional kinematics, are more supportive of the second hypothesis. The analysis of mineral textures provides an improved dataset for the whole sheath fold and increases our understanding of recrystallization mechanisms active in shear zones.

## 1. Introduction

Sheath folds are tongue-shaped non-cylindrical deformation structures with transversal cross sections revealing elliptical-shaped rings or 'eyes' (e.g., Carreras et al., 1977; Quinquis et al., 1978; Minnigh, 1979; Cobbold and Quinquis, 1980; Ramsay, 1980). The hinge line is curved through more than 90° (Ramsay and Huber, 1987; Passchier and Trouw, 2005), with the closure of the sheath oriented parallel to the transport direction (i.e., parallel to the X axes of the finite strain ellipsoid; Alsop and Holdsworth, 2007). The main structural features of sheath folds are briefly summarized as follows: i) they have a conical- or tongue-shape, with limbs closing toward the apex; ii) sections parallel to the Y-Z

plane show a characteristic circular/elliptical shape, forming eye-type folds (for a comprehensive overview of sheath folds, their formation, and characteristics refer to Alsop et al., 2007; Alsop and Holdsworth, 2007, 2012).

However, the influence of different minerals on the development of sheath fold geometries resulting from the passive or active deformation of materials (Alsop and Holdsworth, 2012) lacks clarity and requires further investigation. Passive sheath folding is defined as where the layering plays no part in the mechanics of the folding process (e.g. Cobbold and Quinquis, 1980, p.120), with the sense of shear remaining constant around the fold and across its axial surface (Alsop and Holdsworth, 2012). Conversely, Alsop and Holdsworth, (2012, p.110) stated

---

that active sheath folding is marked by "heterogeneous deformation in which rheologically distinct layering results in the development of local discontinuities about the sheath closure". In order to address the issue of passive and active folding, we investigate the intracrystalline processes behind sheath fold development through a detailed study of the main rock forming minerals by means of complementary fabric analyses and 3D modelling using neutron tomography.

Sheath folds in rocks can form in a variety of tectonic settings, and have been widely reported around the world, including the Armorican massif (Quinquis et al., 1978; Shelley and Bossière, 1999; Aerden et al., 2021), Cap de Creus (Alsop and Carreras, 2007; Druguet et al., 2009; Carreras and Druguet, 2019), the Scottish Highlands (Alsop and Holdsworth, 2006), the Appalachian Mountains (Merschat et al., 2005), the Scandinavian Caledonides (Passchier and Trouw, 2005), the Arctic zone of the Palaeoproterozoic north-eastern Fennoscandian Shield (Mudruk et al., 2022), the Alps (Maino et al., 2021), the Calabrian-Peloritani Orogen in southern Italy (Fazio et al., 2018; Ortolano et al., 2020), the Oman Mountains (Searle and Alsop, 2007), the Himalayan orogen, as well as several Precambrian terrains (e.g., Ghosh et al., 1999). Sheath folds can form in various materials, including ice (Bons et al., 2016), and settings such as salt basins. Here, horizontal flow of salt (e.g. Fiduk and Rowan, 2012; Pérez-Valera et al., 2017) or vertical uplift of salt (diapirism) leads to concentrated shear stresses within the salt and along the interfaces between the salt and adjacent sedimentary rocks (e.g. Jackson et al., 1994; Rowan and Vendeville, 2006; Hudec and Jackson, 2007). For a comprehensive review, refer to Alsop et al. (2007) and Carreras and Druguet (2019). Most commonly, sheath folds are associated with deformation in mountain belts or convergent plate boundaries, but can also form in response to strike-slip faulting or extensional tectonics (Ramsay and Huber, 1987; Passchier and Trouw, 2005). Moreover, sheath folds are typically the result of progressive deformation in complex high strain zones, regardless of the tectonic regime (strike-slip, compressional, extensional, or combinations), and often are the result of polyphase deformation (White, 2010).

Sheath folds develop at a large range of scales (Fazio, 2019) spanning from millimetre-scale, as observed in thin sections (Fazio et al., 2018) up to regional kilometre scale forming megafolds (Alsop, 1994; Rowan and Vendeville, 2006; Searle and Alsop, 2007; Mudruk et al., 2022; for a review of sheath fold scales see Alsop et al., 2007). The ubiquity of sheath folds and the potential link between their shape and strain is one of the main factors behind their extensive previous study, both for their tectonic implications and the link between regional high-strain structures and the structural control of sheath folds' development on ore deposit distributions/creation (Roberts, 1987; Park, 1988; Kampmann et al., 2016; Rozendaal et al., 2017, and references therein; Cawood et al., 2023). For instance, Kampmann et al. (2016) have shown how the rheological contrasts between layers in sheath folds and the related steeply plunging foliations affect not only the localization of ore deposits (e.g., the Cu–Au mineralization of the Falun deposit) but their geometrical 3D patterns (e.g., cone- or rod-shaped geometry).

Sheath folds are usually initiated by a flow perturbation or a general flow instability (see Carreras et al., 2005). Several authors (e.g., Carreras et al., 1977; Quinquis et al., 1978; Minnigh, 1979; Cobbold and Quinquis, 1980; Ramsay, 1980) have suggested that folds with gently curving hinge lines previously nucleated with hinge lines at a high angle to the transport direction and progressively rotated towards it. Such folds, formed about the transport direction, may have this curvature accentuated during progressive simple shear deformation, resulting in highly curvilinear sheath fold geometries. The tectonic history of several regions has been reconstructed from the shapes, mineral distributions, and orientations of folds. As a result, the microstructural features of a sheath fold can therefore provide crucial information about the deformation pathways of the rock layers that are involved. For example, map-scale sheath folds in the southern Appalachians have been used to infer the orientation and magnitude of the bulk strain during mid-crustal flow of the metamorphic core (Merschat et al., 2005). Since Ramsay and Huber

(1987), it has been suggested that sheath folds may develop around: 1) rigid objects within a more ductile rock matrix (Rosas et al., 2002), 2) slip surfaces (Reber et al., 2012, 2013a) or 3) weak inclusions (Reber et al., 2013b; Maino et al., 2021). In such cases, the internal profile of the structure is determined by the shape and size of the inclusion, as well as the deformation history of the surrounding rock (Ramsay, 1967; Carreras et al., 2005).

Sheath folds are examples of complex folding mainly related to non-coaxial shearing (Oriolo et al., 2022), with hinge lines nucleating nearly orthogonal to the shear direction and tending to rotate towards the latter during progressive shearing (e.g., Carreras et al., 1977; Cobbold and Quinquis, 1980; Carreras et al., 2005; Alsop and Carreras, 2007; Schulz et al., 2008; Carreras and Druguet, 2019). Various factors influence the formation of sheath folds, including the mechanical properties of the rocks involved, such as their strength, ductility, and orientation with respect to the direction of stress (Ramsay and Huber, 1983), rheological properties of the rock matrix, the orientation and location of any inclusions, and the direction and intensity of the applied stresses (Alsop and Holdsworth, 2007). For example, in areas of high strain, rocks with different mechanical properties can be subjected to different amounts of deformation and strain. This can lead to the formation of sheath folds, where more competent layers form the sheath and less competent layers form the core (Davis and Reynolds, 1996). Alternatively, if rocks are subjected to compressive stresses that are not aligned with their orientation, they may buckle and fold, leading to the development of sheath folds (Passchier and Trouw, 2005). The formation of sheath folds can also be influenced by the presence of pre-existing structures, such as faults, joints, or foliations. In these cases, the deformation may be concentrated along these features, leading to the formation of sheath folds that follow the orientation of the pre-existing structures (Ramsay and Huber, 1983, pag. 463).

Along with the characterisation of geometric features such as foliation or lineation (e.g., Alsop and Holdsworth, 2006; Alsop et al., 2007; Alsop and Holdsworth, 2012), crystallographic preferred orientation (CPO) of minerals (Fazio et al., 2010; Renjith et al., 2016; Hunter et al., 2018b; Graziani et al., 2020; Nania et al., 2022) is increasingly used to link micro-to-regional-scale deformation. CPO analyses potentially provides information on the orientation and magnitude of the deformation, as well as the rheological response of the rock. The CPO of minerals, particularly quartz and biotite, in metamorphic rocks can provide important information about the deformation history of the rock and the orientation of the strain ellipsoid. Quartz and biotite are both common minerals in medium to high-grade metamorphic rocks, and their crystal structures make them particularly sensitive to deformation. Under conditions of ductile deformation, quartz grains tend to elongate in the direction of maximum stretch and to re-orient accordingly to the active slip systems and deformation processes (e.g. Stipp et al., 2002; Toy et al., 2008; Morales et al., 2011b). The quartz CPO is a function of several factors, including deformation temperature, strain rate, initial grain size, recovery annealing vs. recrystallization of new grains, and the possible development of secondary foliation, such as oblique foliation in mylonitic rocks. A thorough understanding of the CPO necessitates the consideration of all these factors. Similarly, biotite grains tend to align their basal planes perpendicular to the direction of maximum shortening, resulting in a strong SPO and also strong CPO (Punturo et al., 2017).

The CPO of minerals is still poorly investigated in sheath folds, although it is thought to be complex and to vary between different parts of the fold (Morales et al., 2011a; Fazio et al., 2018). For example, in the axial surface region of the fold, quartz grains may exhibit a strong preferred orientation with respect to the fold hinge lines, while on the limbs, the orientation may be more complex and reflect the influence of local finite strain gradients (Crispini and Capponi, 1997). Development of sheath folds and potential triggers for the process have been hypothesized in the literature (e.g., Cobbold and Quinquis, 1980; Reber et al., 2012; Carreras and Druguet, 2019). However, intracrystalline

deformation and rheological behaviour of minerals and their CPOs are not typically taken into account. Major studies on the orientation of minerals have been performed using optical methods, such as U-Stage and fabric analyzer (Schmid and Casey, 1986; Stünitz, 1991; Crispini and Capponi, 1997), and SEM-EBSD (Scanning Electron Microscopy/Electron Back-Scattered Diffraction) based systems (Morales et al., 2011a). These studies have been carried out for limited sampling or grain statistics, mostly due to the limitation of the techniques available at the time. Nowadays spatially resolved EBSD data can be combined with Neutron Diffraction (ND) allowing more robust statistical analyses of mineral CPOs (e.g., Wilson et al., 2022).

The main research questions we pose in this study are:

(a) How does the deformation path vary (or not) within a multi-layer sheath fold?
(b) Do fabric and flow variations develop in different structural positions within a sheath fold?
(c) Can the microfabric be used to determine if a sheath fold is propagating actively or passively?

To answer these questions and obtain a robust three-dimensional picture of a single sheath fold, we have analysed a metre-scale sheath fold originally sampled and described by Alsop and Holdsworth (2012). We explore its full fabric, combining detailed SEM-EBSD analyses of quartz and biotite with neutron diffraction (ND) texture analysis on a series of slices that were cut between the apex and body, and the inner and outer zones of the fold (Alsop and Holdsworth, 2012). To speculate on the possible deformation mechanisms and the differential stress accommodated by quartz in different structural domains, we investigated full CPOs of quartz and biotite, quartz subgrains, and individual phases and bulk kinematic vorticity axes (CVA; Michels et al., 2015) through a combination of crystal fabric analyses (i.e., SEM-EBSD, Neutron Diffractometer). CVA analysis by means of EBSD is a technique used to ascertain kinematic vorticity axis orientation in sheared rocks. It can facilitate comprehension of kinematic partitioning as well as strain localization, both in thin section scale and throughout a field area.

## 2. Geological setting of the sample site

The northwestern extent of the (exposed) Scandian orogeny in Scotland is defined by the easterly-dipping Moine Thrust Zone that separates the foreland (in the west) from the early Neoproterozoic Moine Supergroup further east (Fig. 1a and b) (see Strachan et al., 2020 for a recent summary). The Moine Supergroup rocks are located within a suite of east-dipping Scandian thrust nappes thought to be active at 437-415 Ma (Holdsworth et al., 1994; Strachan et al., 2010, 2020) which along the north coast of Scotland are defined by (from structurally lowest to highest) the Moine, Naver, Swordly and Skinsdale Thrusts (Fig. 1a and b). Additional thrusts exist within the Moine Nappe (Achinver and Ben Hope Thrusts) that do not separate distinct lithologies, although in the case of the Ben Hope Thrust may represent a thermal break marking the Ben Hope Nappe (Thigpen et al., 2013; Ashley et al., 2015) (Fig. 1a and b). The upper part of the Ben Hope nappe, where the sheath fold sample was collected (hanging-wall of BHT, Fig. 1b), has already been constrained by garnet-biotite thermometry to have a peak metamorphic temperature of 675 + 25 °C (Ashley et al., 2015). More recently, Mako et al. (2023, their BH-15-04 sample) estimated a temperature of 593 + 25 °C by calculating the average $X_{Y+HREE}$ content of monazite, which lowers the previously inferred peak temperature by approximately 80 °C. Pressure estimates derived from compositional isopleths of garnet and metamorphic mineral assemblages stability fields inferred by means of pseudosections calculations range between 4 and 8 kbar in the various nappes (Ashley et al., 2015; Ashley et al., 2017).

The sheath fold sample was collected from the Ben Hope Nappe

between the Ben Hope Thrust (BHT) and overlying Naver Thrust (NT) in a tectonic setting marked by NW-directed tectonic transport that generated eye-type fold geometries at various scales (Holdsworth, 1989; Alsop and Holdsworth, 2004; Thigpen et al., 2013, Fig. 1). The BHT (Fig. 1a–c) can be recognized by the juxtaposition of Lewisianoid basement inliers and amphibolites that are thrust to the west over metapsammites within a retrogressed, ~20 m thick simple shear dominated mylonite zone (Holdsworth, 1989; Holdsworth and Grant, 1990; Holdsworth et al., 2001; Thigpen et al., 2013; Graziani et al., 2021). The CPO fabric was significantly affected by the tectonic framework of the sampling site, located between two major thrusts (BHT and NT).

The sheath fold sample used in this study was originally collected and described by Alsop and Holdsworth (2012) from metapsammites and metapelites interlayered on a 10 cm scale, and which form part of the Moine Supergroup (see details in Strachan et al., 2010; Strachan et al., 2020; Lusk and Platt, 2020) (Fig. 1a, b, c). The sample site (Lat., Long. – decimal – 58.484426, −4.3573632) is in the upper part of the Moine Nappe (above the Ben Hope Thrust) in an area associated with top-to-the-NW-directed Scandian thrusting at 435-425 Ma (Holdsworth et al., 2001, 2006, 2007; Mako et al., 2019, 2023; Thigpen et al., 2021) (Fig. 1a, b, c). Sheath folds develop at cm-to km-scales throughout the area and are marked by increasing non-coaxial deformation towards high strain zones (see Holdsworth et al., 2001; Alsop and Holdsworth, 1993; Alsop et al., 1996, 2010, 2021). The quartzo-feldspathic Moine metapsammites contain a regional foliation (S2) defined by aligned quartz and biotite that dips towards the SE, and a gently SE-plunging regional lineation (L2), that are folded around the nose of the sampled sheath fold (Fig. 1c). The regional foliation (S2) and lineation (L2) developed during top-to-the-WNW regional D2 thrusting, with folding of these fabrics by the sheath fold suggesting that it formed relatively late (locally F3) during progressive D2 shearing (Alsop and Holdsworth, 1993, 2012; Alsop et al., 2010). The sampled sheath fold is a tight synform with a slightly steeper dipping upper limb, that closes towards the SE, and displays 120° of hinge-line curvature around the trend of the regional lineation (L2). Alsop and Holdsworth (2012) show that axial surfaces are curvi-planar and have a consistent sense of obliquity relative to the Z axis with angles varying both in cross sections of the sheath as well as along its length. The consistent obliquity of axial planes relative to the foliation (S2) may result in S3 transecting the sheath fold hinge, explaining why the intersection lineations "wrap" obliquely around the fold hinge. The investigated sheath fold has a maximum dimension of approximately 35 × 15 cm along the Y and Z axes of the largest eye-shaped section (15a in Fig. 2c) cut parallel to the Y-Z plane (for precise dimensions, see Fig. 2a–c, 3). The sheath fold is considered to have originally formed the lower limb of a NW-verging fold pair, such as are developed throughout the area (e.g., Holdsworth et al., 2001).

## 3. Materials and methods of textural analysis

The sample consisting of quartz-feldspar-biotite metapsammite was serially sectioned using a commercial rock saw with a 6 mm thick blade, at 15–20 mm intervals along the length (X axis) of the sheath fold and normal to the (X–Y) axial plane (Fig. 2; see Alsop and Holdsworth 2012 for details). The resulting eye-shaped closure patterns were then geometrically investigated by Alsop and Holdsworth (2012). We have now made thin sections from the sheath fold slices in different micro-domains (Figs. 3 and 4) normal to the elongation (X axis of the finite strain ellipsoid) and at right angles to the (X–Y) axial plane for microstructural analysis. While thin sections have been cut both parallel to Y-Z (used for classical petrographic observations to see general microstructures) and X-Z, however only those cut parallel to the X-Z plane have been used for EBSD analyses (Fig. 3).

A digital virtual 3D model was constructed using Move 2020.1.10 geomodelling software package (Petex Ltd.) with folded foliation planes manually traced on both sides of rock slices surfaces (i.e., marker traces,
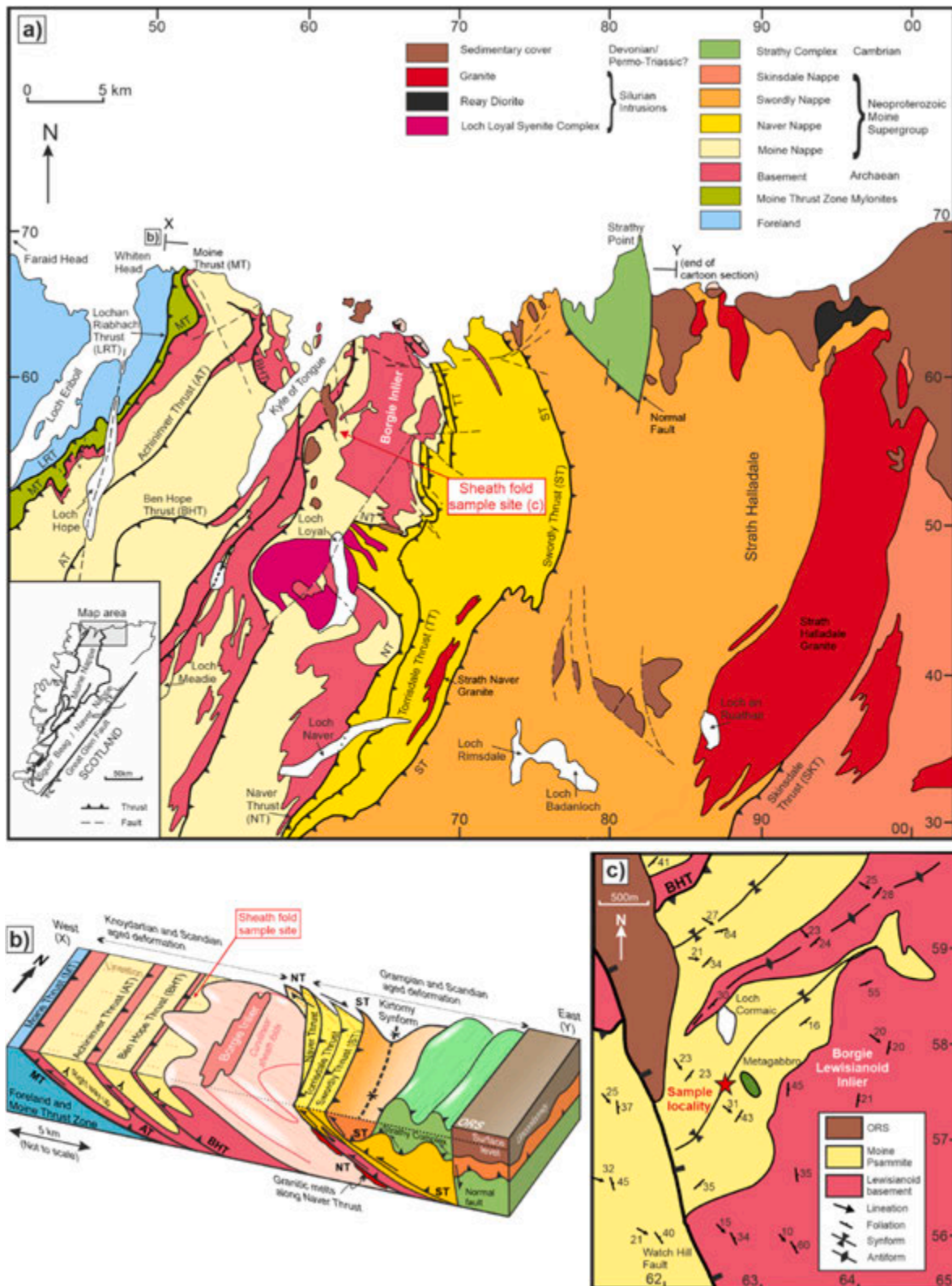
**Fig. 1.** (a) Geological map of the northern Scottish Highlands with sample location (modified from Alsop et al., 2021). (b) Schematic cross-section (see a for location and orientation) (modified after Alsop et al., 2021). (c) Detailed geological map of the study area (red star marks the sheath-fold sample location; modified from Alsop and Holdsworth, 2012). Legend: AT Achness Thrust, BHT Ben Hope Thrust, NT Naver Thrust; the sheath fold is located within the Ben Hope thrust sheet/-nappe. (For interpretation of the references to colour in this figure legend, the reader is referred to the Web version of this article.)
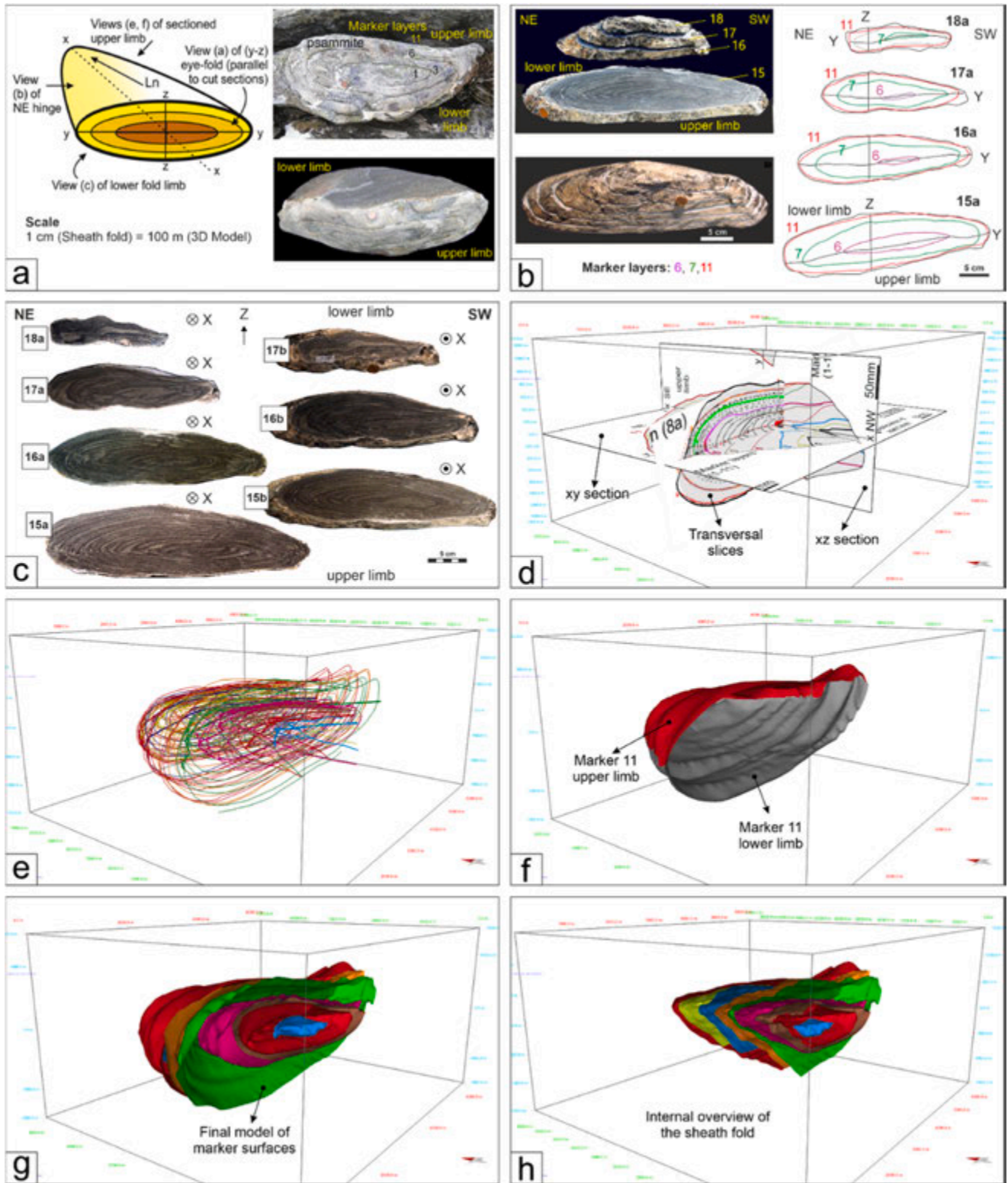
**Fig. 2.** (a) Back (top right) and upper (bottom right) views of the collected sample (Alsop and Holdsworth, 2012) and sketch model (left) of the sheath fold. (b) The four slices (15, 16, 17, 18) where microdomains have been selected for textural analyses (marker layers 6, 7, and 11 are shown as red, green and purple lines, respectively). (c) Photograph of polished surfaces of slices 15, 16, 17, and 18 used in this study (labels a and b refer to the larger downside and smaller upside faces of the same slice, respectively). (d) 3D view of orthogonal sections and transversal slice 8a. (e) 3D view of picked markers within all the transversal sections. (f) Construction of 3D marker surfaces n°11 (see Supp. Fig. 1). Upper and lower limbs are developed separately and successively merged together. (g) 3D view of all the nine modelled marker surfaces. (h) 3D view (clipping view) showing the internal structure of the sheath fold (marker layers used are the same traced by Alsop and Holdsworth, 2012). (For interpretation of the references to colour in this figure legend, the reader is referred to the Web version of this article.)
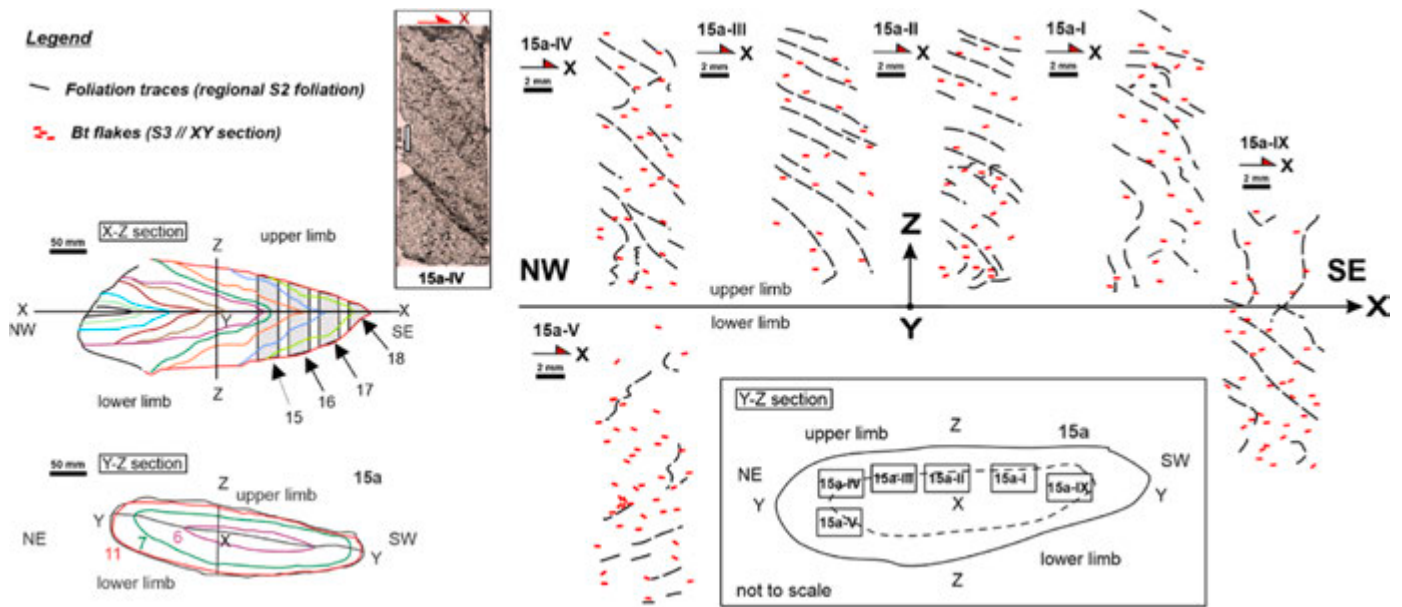
**Fig. 3.** Schematic sketch of folded regional foliation (S2) defined by alternating quartz- and mica-rich layers (traces are inferred from scanned thin sections cut parallel to the X-Z plane). The biotite flakes with their (001) planes define a new axial plane foliation (S3) developed mainly along the X–Y section. Red arrows point to the SE closing sheath fold (X direction). (For interpretation of the references to colour in this figure legend, the reader is referred to the Web version of this article.)
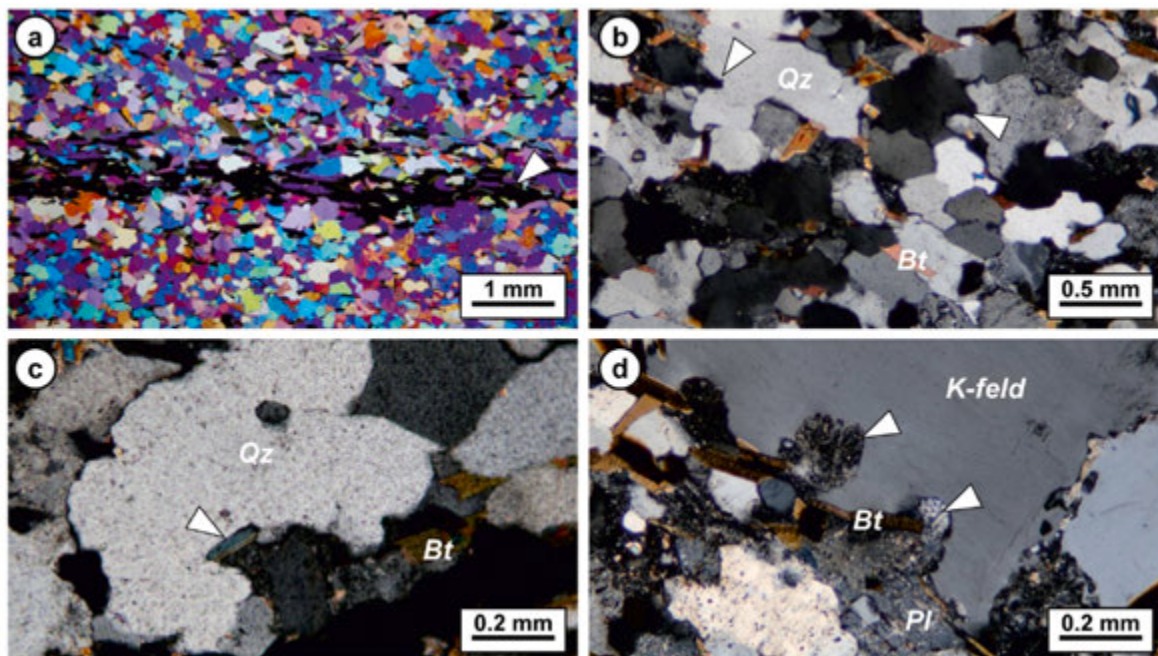


**Fig. 4.** Overview of microstructures within the studied metapsammite. a) Panoramic of biotite flakes defining the main foliation (S2) as seen along Y-Z plane of finite strain ellipsoid (crossed-polarizer light with lambda plate). b) Irregular, lobate quartz grain boundaries (arrow), indicating dynamic recrystallization in the grain boundary migration regime for quartz (crossed-polarizer light). c) Pinning microstructure (arrow) of quartz grain boundaries on biotite (crossed-polarizer light). d) Myrmekite growth (arrow) along K-feldspar grain boundary (crossed-polarizer light). Mineral abbreviations: Bt - biotite, K-Feld - K-feldspar, Pl - plagioclase, Qz - quartz.

Fig. 2). The 3D model (Fig. 2 e-h) file is also available for download via supplementary materials. Modelling was based on two orthogonal sections cutting across the sheath fold (X–Y and X-Z sections, representing the horizontal and vertical-longitudinal sections respectively, Figs. 2a) and 14 transversal slices (27 faces considering the front and back of each slice). To evaluate in detail the textural and kinematic variations recorded by quartz and biotite during folding, we analysed different portions of the sheath fold by electron backscatter diffraction (EBSD)

and Neutron Diffraction (see Hunter et al., 2017a, b; Fazio et al., 2017 for comparison).

### 3.1. Fabric microanalysis

EBSD and ND can be considered two complementary techniques in the textural analysis of geomaterials. EBSD enables great analytical detail while maintaining structural control by examining "small" areas

(one usually does not map more than an entire thin section for practical and time issues). With ND, large volumes are analysed providing the full-fabric with greater statistics; however, without being able to verify which structural domains are being scanned within the volume (Fazio et al., 2017; Hunter et al., 2017b). This runs the risk of including grains that should be discarded from the calculation, such as those grains surrounded by second-phase minerals or those influenced by variations in the orientation of the 3D foliation plane. Comparing the two datasets is the best way to obtain a quantitative result while considering the heterogeneities of the sample. Moreover, ND is particularly suitable for acquiring the biotite fabric, as it avoids some indexing problems related to polishing (e.g., poor indexing, noise reduction, and pseudo-symmetry removal) and it investigates more crystals.

We also note that in this study, we only investigated the apical part of the overall sheath fold (slices 15, 16, 17, 18; see Fig. 3) where the extruding core is only partially preserved (i.e. marker layer 6). We have therefore avoided complexities due to doubling of fold cores (double eye-type pattern) in the opening part of the fold, as well as the occurrence of internal detachment surfaces that disarticulate the enveloping concentric layers near the lower limb. This may explain the low inhomogeneity within the mineral CPO fabric, and this study can thus be considered a first attempt to characterize the relatively simple apex of sheath fold closures.

### 3.1.1. Electron back-scattered diffraction

The EBSD analysis was carried out to acquire "in-situ" crystallographic orientations data of quartz and biotite as a function of the structural domain and to obtain quantitative grain size data. Thin section preparation for EBSD and initial petrographic imaging were carried out at the Fabric Analysis Lab (FAL), Department of Geology and Geophysics, Indian Institute of Technology (IIT), Kharagpur (India). Thirteen oriented thin sections approximating the X-Z plane of the fabric were investigated.

(X parallel to mineral stretching lineation, Z normal to foliation plane) were investigated.

To obtain a damage free surface for EBSD analysis, the final stage of thin section preparation involved polishing with non-crystallizing colloidal silica solution for 6 h. EBSD patterns were acquired at 30 kV accelerating voltage, $1.49 \times 10^{-6}$ mbar system vacuum, and ~17 mm working distance using Carl Zeiss Auriga Compact FEG-SEM fitted with an Oxford instruments NordlysMax2 EBSD detector housed in the Central Research Facility (CRF, IIT Kharagpur, India). Quartz orientation data (Figs. 5–10) were acquired automatically using the software Aztec HKL (Oxford instruments). The data cleaning and initial processing was carried out using the software Aztec Crystal (Oxford instruments) while the final processing of the EBSD data was performed using the MTex toolbox (mtex-toolbox.github.io) for the software Matlab (www.mathworks.com). Grain size maps of quartz were produced along with lower hemisphere spherical equal area projections (pole figures) of the main crystallographic direction of quartz and biotite. The grain size maps were constructed using a grain boundary threshold of 10° to unambiguously highlight grain and subgrain boundaries (e.g., see Fig. 7a–d) while the pole figures were contoured using a de La Vallée Poussin kernel function with a halfwidth of 10°. A detailed study of the subgrain density was performed using the method proposed by Goddard et al. (2020) to quantify the intracrystalline differential stress. This analysis was done using a subgrain threshold of 1°, a Burgers vector of $5.1 \times 10^{-4}$ μm, and a shear modulus of $4.2 \times 10^4$ MPa (see Goddard et al., 2020 for more details). Density analyses on the peripheral areas of the quartz c-axis pole figures were carried out using the quantitative method of Hunter et al. (2018a).

### 3.1.2. Neutron diffraction

Neutron Diffraction (ND) analyses were performed to refine and expand biotite and quartz textures from the EBSD dataset. Due to the
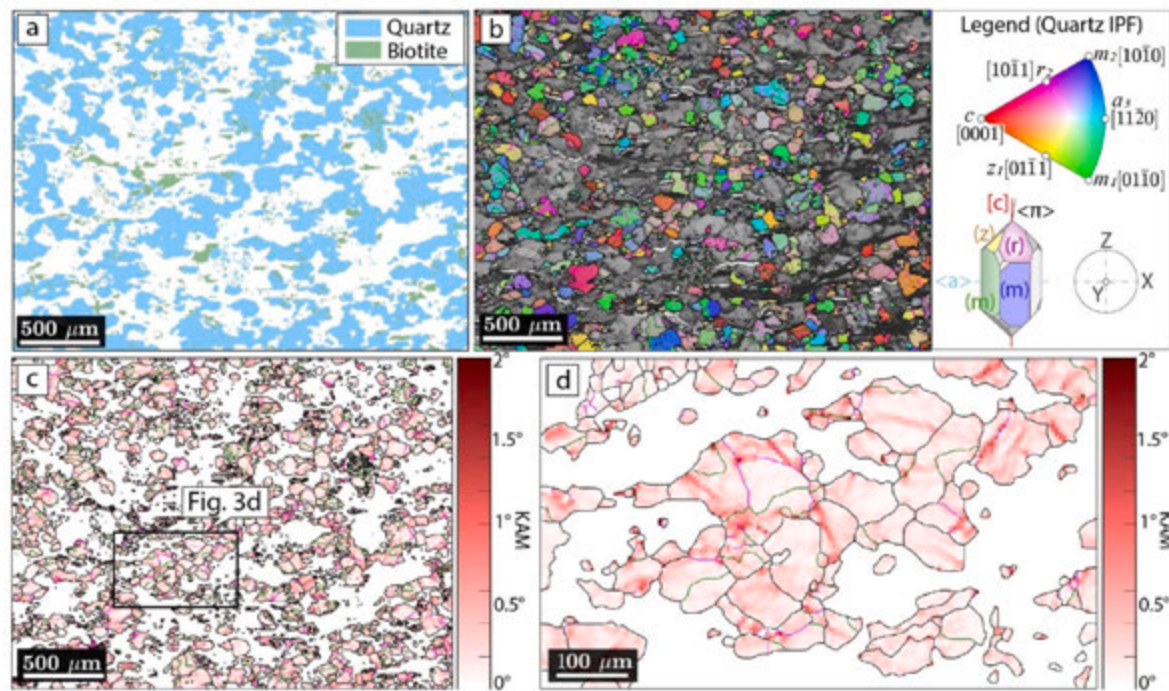


**Fig. 5.** Example of elaborated SEM-EBSD maps (sample 16a-I; see Supplementary materials for the complete dataset). a) Phase map, showing quartz and biotite grains; white areas correspond to other mineral phases. b) Inverse pole figure map of quartz, showing internal subgrains (delimited by purple lines) and Dauphiné twinning (green lines). The colours of the grains in the map correspond, in the legend to the right, to the crystallographic orientation of quartz grains compared to the direction of the lineation (corresponding to the X-axis of the finite strain ellipsoid of the sheath fold), and can be directly visualized as crystal face orientation. c) Kernel Average Misorientation (KAM) map for quartz grains. The red gradient indicates misorientation grade among neighbour pixels. Subgrains (>2°) are highlighted by purple lines, Dauphiné twinning by green lines. White areas correspond to second-phase minerals. d) subset of the KAM map c). (For interpretation of the references to colour in this figure legend, the reader is referred to the Web version of this article.)
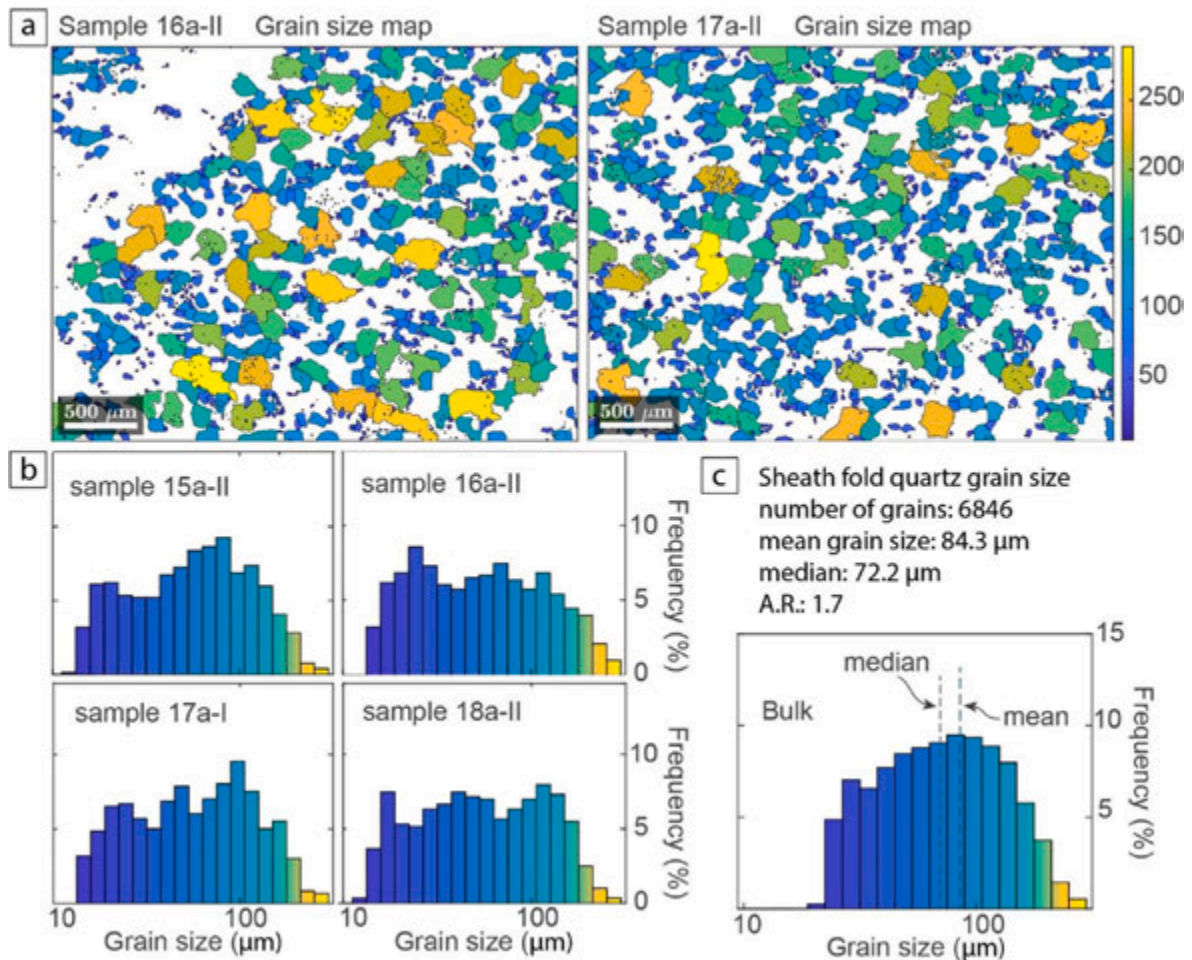
**Fig. 6.** (a) Examples of quartz grain size maps (based on SEM-EBSD data) of two areas representative of two different sheath fold slices. The colour-coded calibration bar indicates the radius of the grain equivalent circle (μm). (b) Examples of grain size distribution histograms for representative areas of the four studied sheath fold slices (logarithmic scale for the grain size axis). (c) Quartz grain size distribution histogram for the bulk sheath fold (after noise removal), showing the mean and the median grain size (logarithmic scale for the grain size axis). A.R. is the mean aspect ratio of quartz grains of the bulk sampling. See Supplementary materials for the complete dataset. (For interpretation of the references to colour in this figure legend, the reader is referred to the Web version of this article.)

neutron's large penetration capabilities (Feldmann, 1989; Vogel and Priesmeyer, 2006), the ND texture represents the bulk average texture over the whole sample volume, while the EBSD is limited to data from a single cross-section surface data. Thus, ND has the advantage over other techniques of large grain statistics and high fidelity of data. Investigation was performed at the Australian Centre for Neutron Scattering (ANSTO, Sydney). ND textural analysis has been performed on rock samples extracted from two slices, 15a and 17a (Figs. 11 and 12), to reconstruct volumetrically representative quartz and biotite CPOs. Small cubes approximately $10 \times 10 \times 10$ mm in size were extracted from different representative locations within the fold with potentially different deformation features and therefore textural characteristics (Figs. 11 and 12). A series of nine representative specimens allow us resolving the spatial distribution of deformation across the investigated fold.

Textural data have been acquired by means of the Kowari neutron diffractometer (for instrument reference see Garbe et al., 2015). For measurements of quartz and biotite multiple pole figures, the wavelength of 2.5 Å and three detector (Bragg angle) position, $2\theta = 39°, 64°,$ $92°$ (each with coverage $\pm 7°$) were used to acquire partial diffraction patterns covering the most desired diffraction peaks. As a result, 9 pole figures of quartz were extracted from the mentioned detector positions: (100), (101)/(011), (110), (102)/(012), (111), (112), (003), (202)/(022), (103)/(013) as well as several pole figures of biotite. All

measurements were performed on a regular $35° \times 35°$ spherical grid to maximize the grain statistics – with such a fine mesh all grains in the sample are guaranteed to be detected.

The orientation distribution functions (ODFs) were reconstructed combining the ND orientation data for quartz and biotite in each sample using the MTex toolbox adopting the de La Vallée Poussin kernel function with a halfwidth of 10°. The following lattice parameters were adopted: a = b = 4.9 Å, c = 5.4 Å, $\alpha = \beta = 90°$, $\lambda = 120°$, point group '321' for quartz; and a = 5.3 Å; b = 9.3 Å, c = 10 Å; $\alpha = \lambda = 90°$, $\beta = 100.23°$, point group '12/m1'. The lower hemisphere pole figures of the most relevant crystallographic axes and planes have been recalculated for quartz and biotite and plotted using the XZ plane of the finite strain ellipsoid as the projection plane, with a contouring halfwidth of 10°. For quartz and biotite CPOs intensities, the texture index (or J-index) of Bunge (1982) and the M-index of Skemer et al. (2005) were calculated (see Table 1 for EBSD data and Table S1 for Neutron Diffraction data).

*3.1.3. Crystallographic vorticity axis*

Furthermore, crystallographic vorticity axis (CVA) analysis (Fig. 10) was performed on quartz, biotite and the bulk grains using EBSD outputs to extrapolate the orientation of the vorticity axis, matching the intragranular dispersion of internal crystallographic orientations of each grain of the aggregate. Indeed, according to Michels et al. (2015), in sheared polymineralic aggregates, the population of the CVAs point to
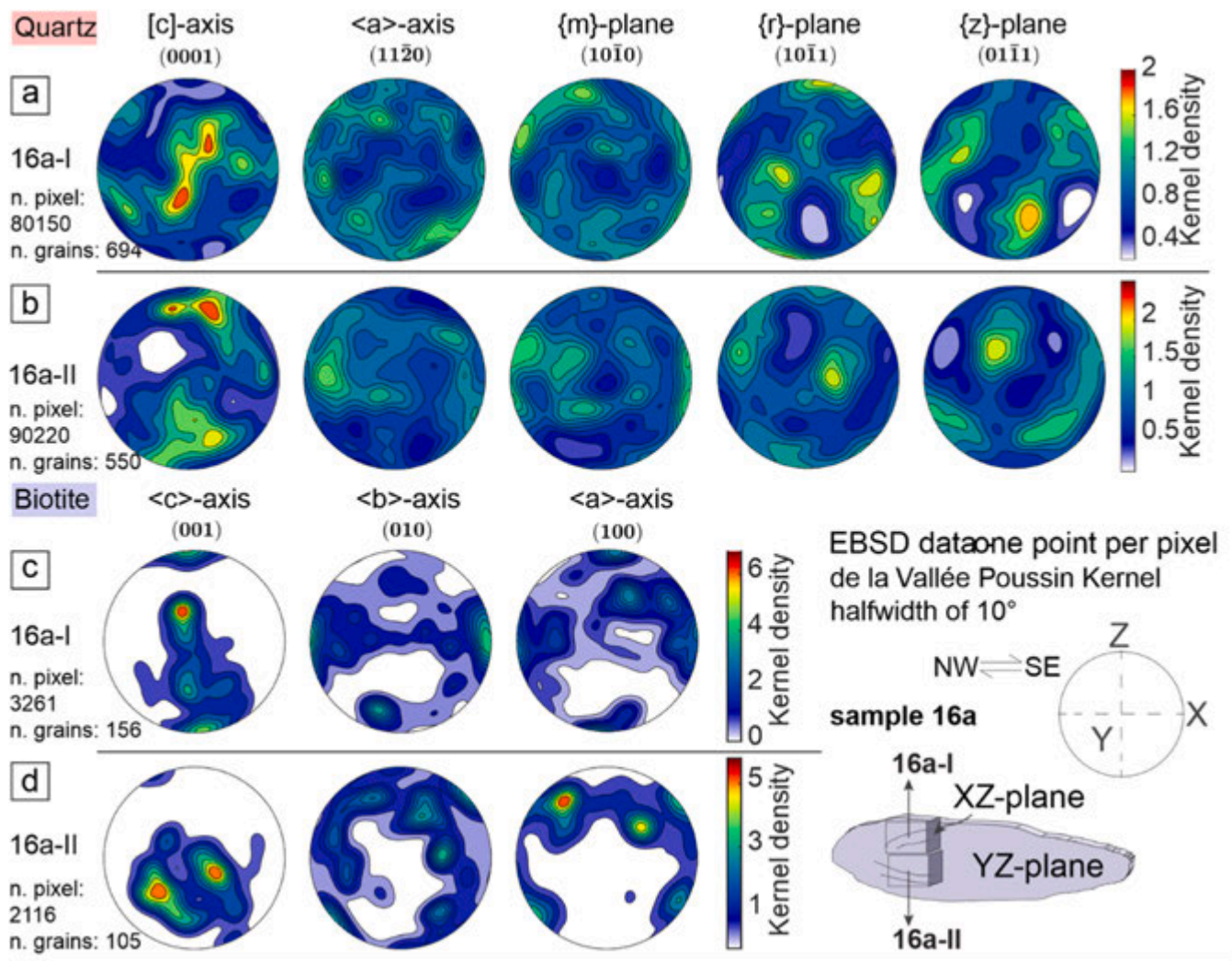
**Fig. 7.** Quartz and biotite pole figures (lower hemisphere, equal area projection) of two representative areas of the sheath fold, based on EBSD data. All texture projection planes are sections oriented parallel to the XZ-plane of the finite strain ellipsoid with respect to the flattening direction of the sheath fold. Colour bar scales indicate multiples of uniform distribution of the de la Vallée Poussin Kernel function (Schaeben, 1997) with a halfwidth of 10° (Hielscher and Schaeben, 2008). Supplementary materials for the complete dataset. (For interpretation of the references to colour in this figure legend, the reader is referred to the Web version of this article.)

the orientation density of the bulk vorticity vector in shear zones, regardless the tectonic regime and kinematic flow, vorticity, and macroscopic fabric elements such as lineation, foliation.

### 3.2. Neutron tomography

To characterize the three-dimensional bulk distribution of minerals in the series of nine cube samples, a neutron tomography (NTO) study was conducted. The NTO measurement was performed on the imaging beamline Dingo at ANSTO (Garbe et al., 2015). The high-resolution configuration, corresponding to a L/D ratio of 1000 (where L is the distance between the beam collimator to the image plane, and D the diameter of the collimator) was used. The analysis was conducted with a ZWO ASI2600MM Pro (6248 × 4176) CMOS sensor camera coupled with a 100 mm lens to yield images with a pixel size of 17 μm. The detector system was equipped with a 30 μm thick Gd2O2S:Tb scintillation screen. The tomographic scan was carried out with an equiangular step of 0.17° over 360° and an exposure time of 90s each. Flat field normalization with dose correction, dark current subtraction, ring artefacts suppression in frequency and real space domains were applied to the raw data. The neutron tomography stacks were computed using the

NeuTomPy toolbox (Micieli et al., 2019). The Avizo 2020.3.1 software was employed for data visualization and evaluation (https://www.thermofisher.com/au/en/home/electron-microscopy/products/software-em-3d-vis/avizo-software.html accessed on January 24, 2023).

To enhance the quality of the NTO image, anisotropic diffusion (AD) and unsharp mask (UM) filters were applied via AVIZO. The noise-reduction AD filter merges regions of similar grey-scale values and intra-region smoothing is promoted over edge smoothing. The blurring introduced by the AD filter was reduced by UM filter to reinforce the contrast at edges.

Different mineral phases can feature variations in neutron attenuation intensity that displays as grey-tone values in the NTO reconstructed slices. Based on grey values, phases can be virtually separated through threshold segmentation. In the segmentation each pixel in the slice images composing the NTO stack is assigned to a label which describes the region or minerals associated with the pixel (e.g., Qtz, K-feld, Bt) within a defined range of grey-tone values. Then the segmented components can be further manipulated and evaluated (Reddy, 2018).
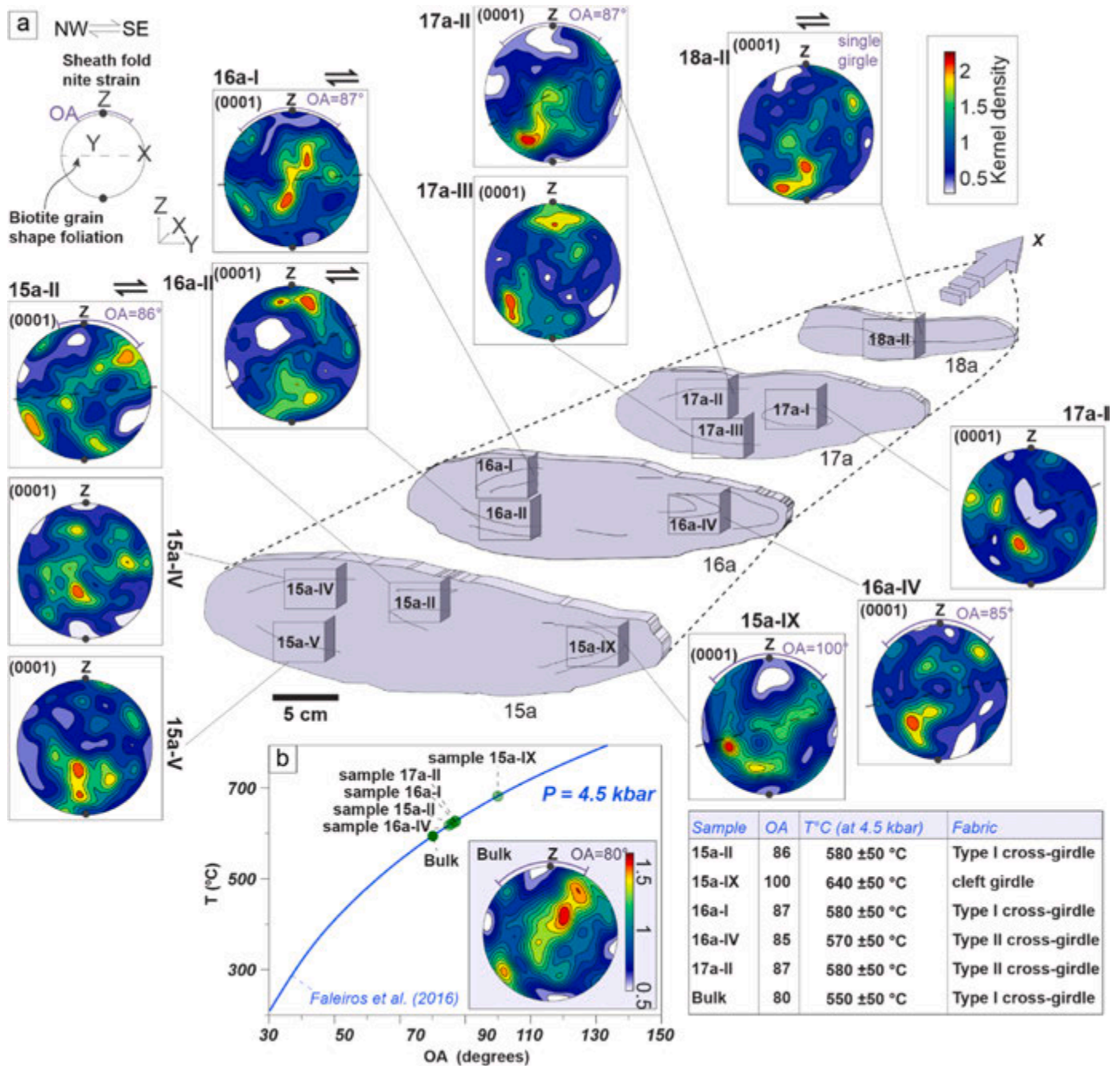
**Fig. 8.** (a) Quartz c-axis pole figures (based on EBSD data, lower hemisphere, equal area projection). All texture projection planes are oriented parallel to the X-Z plane of the finite strain ellipsoid with respect to the flattening direction of the sheath fold itself. Colour bar scale (top right box) indicates multiples of uniform distribution of the de la Vallée Poussin Kernel function. When possible, the foliation plane marked by biotite (within the sheath fold) is plotted (grey dashed line) accounting mica grain shape orientation, at the microscale, and its CPO (e.g., see Fig. 5c and d for biotite CPOs). (b) Quartz pole figures (EBSD) and bulk opening angle (OA) measured on crossed girdle patterns; PT diagram showing OA results (plotted blue line after Faleiros et al., 2016). In the bottom right corner, a table summarizing temperatures inferred from quartz OA. (For interpretation of the references to colour in this figure legend, the reader is referred to the Web version of this article.)

## 4. Results of microstructural and textural analysis

### 4.1. Microstructures

Polished thin sections were analysed by optical microscopy. The main foliation (S2) marked by micaceous layers forms the elliptical traces visible on YZ planes and is well developed in all investigated domains (Figs. 3 and 4). A secondary axial planar foliation (S3) is developed mainly along the XY plane and consists of aligned elongated

quartz grains and is highlighted by the shape preferred orientation of biotite flakes (Fig. 4a). There is no significant variation of microstructures, as well as of mineralogical assemblage and of minerals grain size, across the different slices. The studied metapsammite contains quartz, feldspars, biotite, white mica (phases are listed according to a decreasing of their relative modal abundance) with opaques, zircon, apatite and epidote as accessories phases. Minor chlorite is observed as alteration of biotite, sericite is locally observed in feldspars. Quartz shows evidence of dynamic recrystallization within the grain boundary
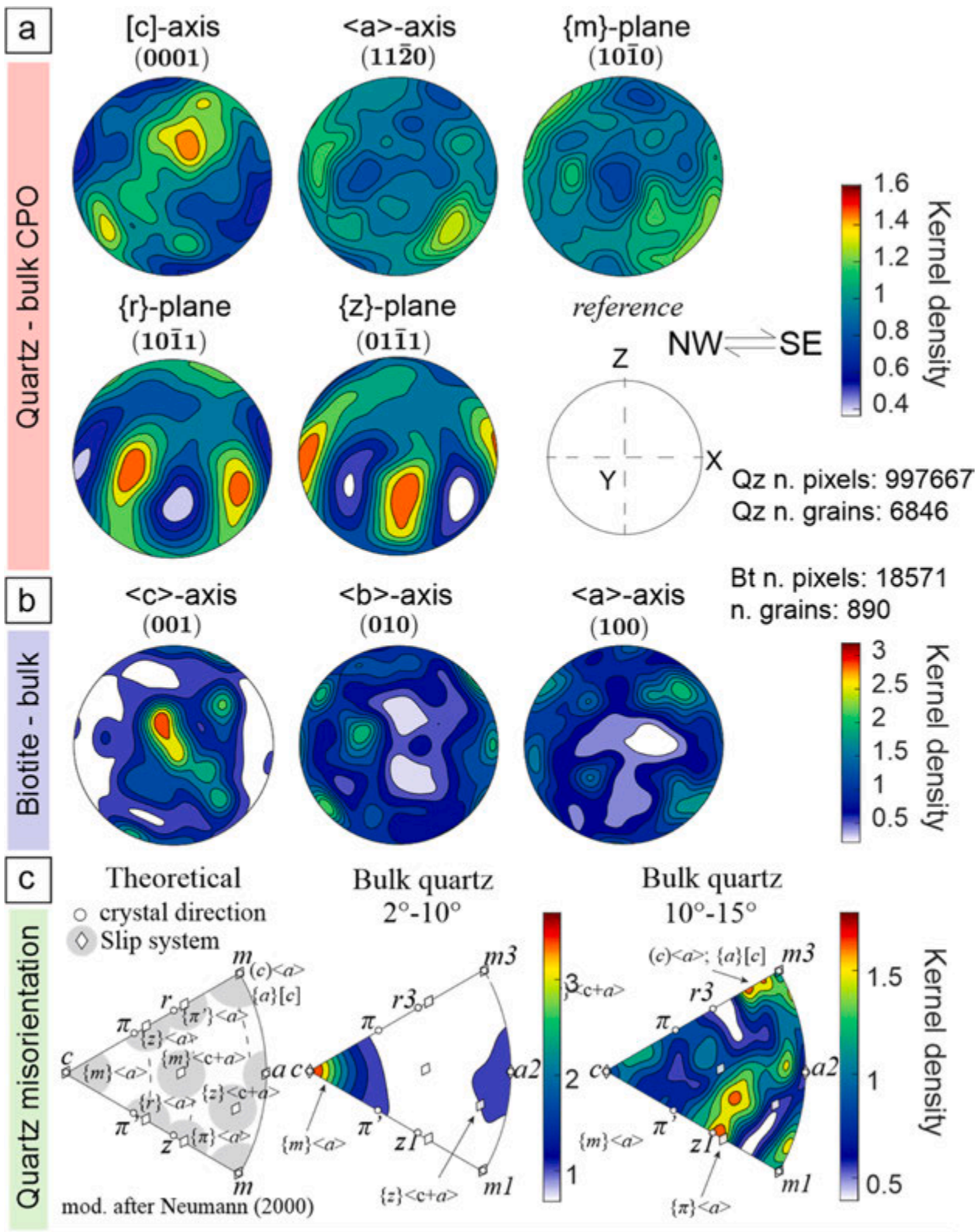
**Fig. 9.** (a) Quartz and (b) biotite pole figures (one point per pixel) for the sheath fold analysed areas (lower hemisphere equal area projection, projection planes are oriented parallel to the X-Z plane) after EBSD analysis. (c) Inverse pole figure of the quartz misorientation axes for slip systems interpretation (modified after Neumann, 2000; Wheeler et al., 2001), and quartz misorientation axes plot for the bulk analysed areas (rotation axes associated with subgrain domains for threshold misorientations angles of 2°–10°; grain boundaries for threshold misorientations angles between 10° and 15°). All colour bar scales indicate multiples of uniform distribution of the de la Vallée Poussin Kernel function. (For interpretation of the references to colour in this figure legend, the reader is referred to the Web version of this article.)
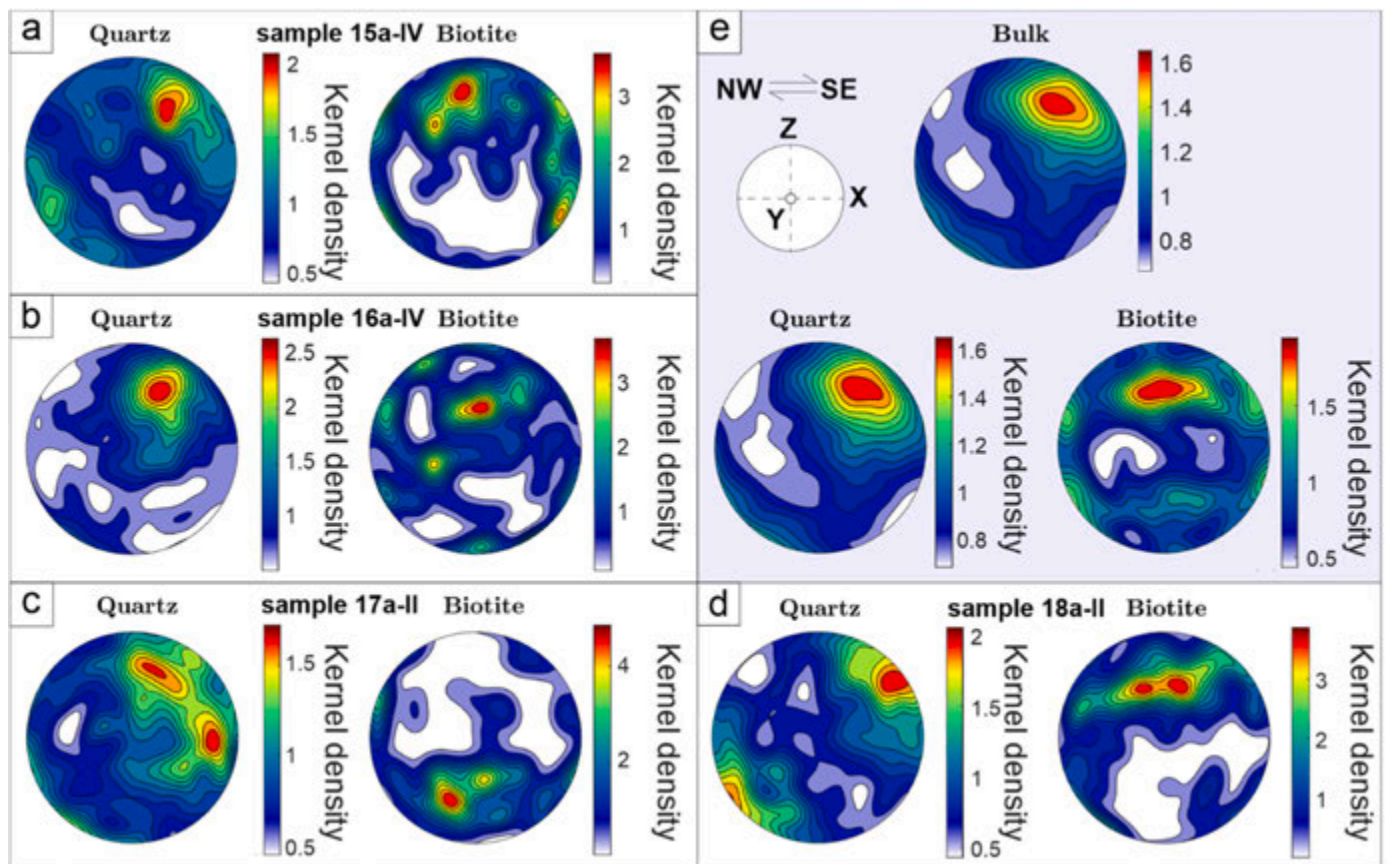
**Fig. 10.** (a-d) Examples of quartz and biotite kinematic vorticity axis (CVA) plots (using EBSD outputs) for selected areas of the slices of the sheath fold (see Supplementary materials for the complete dataset). (e) CVA orientation plots for the combination of quartz and biotite orientations (bulk plot) and for the bulk analysed quartz and biotite (representative for the entire analysed volumes of the sheath fold). All pole figures are in sample coordinates: lower hemisphere equal area projection; projection planes oriented parallel to the XZ plane; reference in (e). Colour bar scales indicate multiples of uniform distribution of the the de la Vallée Poussin Kernel function. (For interpretation of the references to colour in this figure legend, the reader is referred to the Web version of this article.)

migration I regime, GBM$_I$, of Stipp et al. (2002), as indicated by the occurrence of irregular, highly lobate grain boundaries (Fig. 4b) and of windows and pinning microstructures (Fig. 4c). Quartz is only partly interconnected and often in contact with second phases (Fig, 5a, b; Fig. 6a and b), yet it defines a weak phase accommodating the deformation together with biotite. Quartz grain size is homogeneous within the sheath fold (see Fig. 6 for examples, see also supplementary materials A). Feldspars shows evidence of crystalline plasticity as highlighted by undulose extinction, deformation twins in plagioclase and local myrmekite in K-feldspar (Fig. 4d).

### 4.2. CPO (integrated EBSD and ND textural analyses)

Quartz and biotite CPO pole figures from EBSD (Figs. 7–9) and ND investigations (Figs. 11 and 12) show similar patterns, with no significant variations in the fabric strength (expressed by the J and M indexes) across the structure (Table 1, and Table S1). Quartz c-axis pole figures vary from single girdle/incomplete cross-girdle type 1 to hybrid of cleft-girdle and cross-girdle type 2 distributions (Fig. 7a–b, 8, 11, 12). Minor differences between CPOs from EBSD (Figs. 7–9) and ND analyses (Figs. 11 and 12) are related to grain statistics, and minor internal heterogeneities. We interpret quartz patterns as resulting from plane to constrictional strain (Schmid and Casey, 1986). Asymmetries of quartz CPOs, even if they are not particularly well defined in a few cases, mostly suggest a top-to-the-SE non-coaxial flow (i.e. towards the sheath fold apex parallel to the X direction), regardless of the structural position (i.e., the apex or the body of the sheath fold; the outermost or the innermost ellipse, see Fig. 8a). It is noteworthy that both of the fabric

analysis techniques provided us with statistically robust CPO data representative for the quartz CPOs produced by the interaction with all the mineral phases. Therefore, our CPOs (and opening angles, Fig. 8b) are not as refined as they could have been when sampling quartz grains not affected by second-phase minerals (e.g., with a Universal Stage). Our approach is intended to provide an overall appraisal of the deformation recorded within a sheath fold.

The main a-axis maxima of quartz are preferentially oriented parallel to the lineation, while the poles of r-planes are statistically oriented parallel to the pole of the foliation (Fig. 5a and b). The orientations of r-planes and a-axes within individual specimens (Fig. 5a and b) and for the bulk sheath fold (Fig. 9a) indicate deformation by dislocation creep mainly accommodated by rhomb-a slip (for references, see Toy et al., 2008). The cross-girdle distribution of quartz c-axis and the distribution of low angle misorientation axes (Fig. 9c) also indicate the activity of other slip systems which can be identified as basal-a, and π-a (Neumann, 2000).

ND tomography reveals that in the various samples analysed from different portions of the sheath fold, there is little variation in the phases present and the mineral volumes remain essentially unchanged within the volumes analysed (Fig. 13; see supplementary materials for a complete dataset of ND tomography samples). Biotite, defining the foliation within each specimen, is characterized by consistent EBSD and ND pole figures (Fig. 7c–d and Figs. 11 and 12). Couples of c-axis maxima (001) are sub-parallel to the sheath fold X–Y plane of the fabric, indicating variations of the internal foliation orientation across the Y axis of the structure. Minor girdle distributions within the c-axis pole figures are normal to the internal foliations. The poles to the a-axes (100) and b-
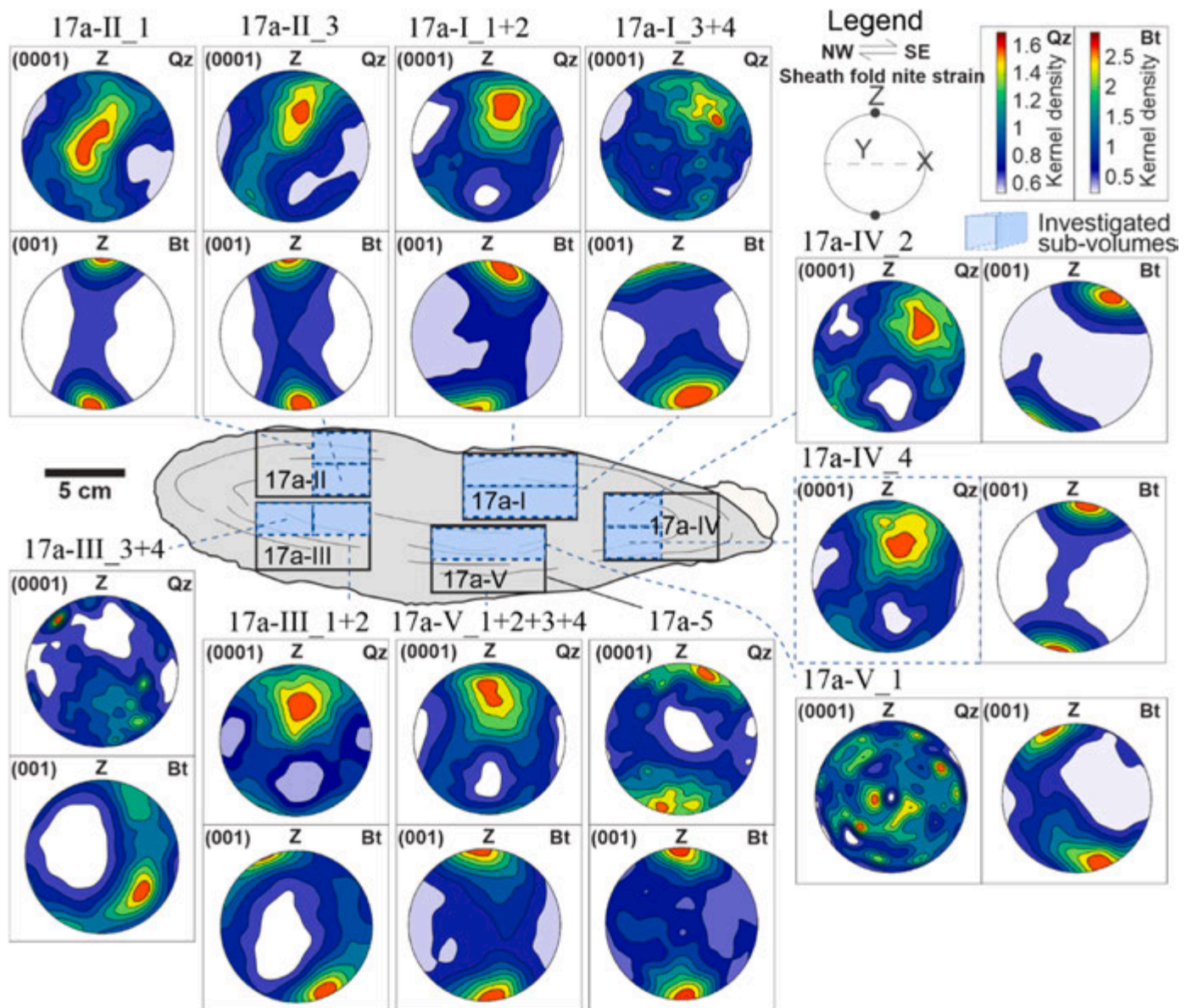
**Fig. 11.** Pole figures for quartz (Qz) and biotite (Bt) textures measured by means of ND (Neutron Diffraction) technique for the 17a slice (different investigated sub-volumes are indicated).

axes (010) define girdle distributions with sub-maxima of the b-axes parallel to the lineation. These distributions, especially considering the c-axis patterns, are constant (see also Fig. 9b for bulk biotite CPO), likely indicating a progressive growth of biotite during folding, with a stronger (re)crystallization at the last increment of deformation. Alternatively, biotite patterns could be associated with passive folding of the foliation during the development of the sheath fold.

### 4.3. Deformation temperature, paleo-stress estimates, and flow regime

Contoured pole figure symmetries of quartz c-axis patterns forming fabric 'skeletons' may be used as a geo-thermometer by analysing the opening angles between maxima of clustered orientations (Kruhl, 1996; Morgan and Law, 2004; Law, 2014). We applied the semi-quantitative method proposed by Hunter et al. (2018a) to compare the fabric intensity spectrum of girdle topologies. The quartz c-axis opening angles (measured by means of the open-source Matlab® toolbox MTEX – script modified after Hunter et al. (2018a) - for samples analysed through the EBSD, see Fig. 8b) range from 84° to 87° with a single outlier of 100°

(15a-IX). During the formation of sheath folds, it can be inferred that the pressure reached 4.5 kbar, coinciding with the thermal peak of regional metamorphism (Thigpen et al., 2013). The deformation temperatures, ranging between 570 ± 50 °C and 580 ± 50 °C, are indicated by the measured opening angles, as presented in Table S2. Sample 15a-IX's opening angle denotes a deformation temperature of 640 ± 50 °C, which still falls within the overall error range of the other results. Thigpen et al. (2013) have inferred from the same area (hanging-wall of the Ben hope Thrust, see their Fig. 4b) temperatures ranging from 565 °C to 680 °C by applying quartz c-axis fabric opening angle thermometry. The opening angle of the bulk quartz CPO is likely underestimated as it accounts for the different rotations of the fabric skeleton of each rock slice. However, amphibolite facies deformation temperatures are also consistent with the GBM regime observed in the quartz (Stipp et al., 2002; Law, 2014) and by the ductile deformation in feldspars (see Passchier and Trouw, 2005). Similar temperature values have also been recently inferred by Southern et al. (2022) who studied elongated quartz pebbles in the Moine Nappe further to the northwest.

The crystallographic vorticity axis (CVA) of quartz and biotite in the
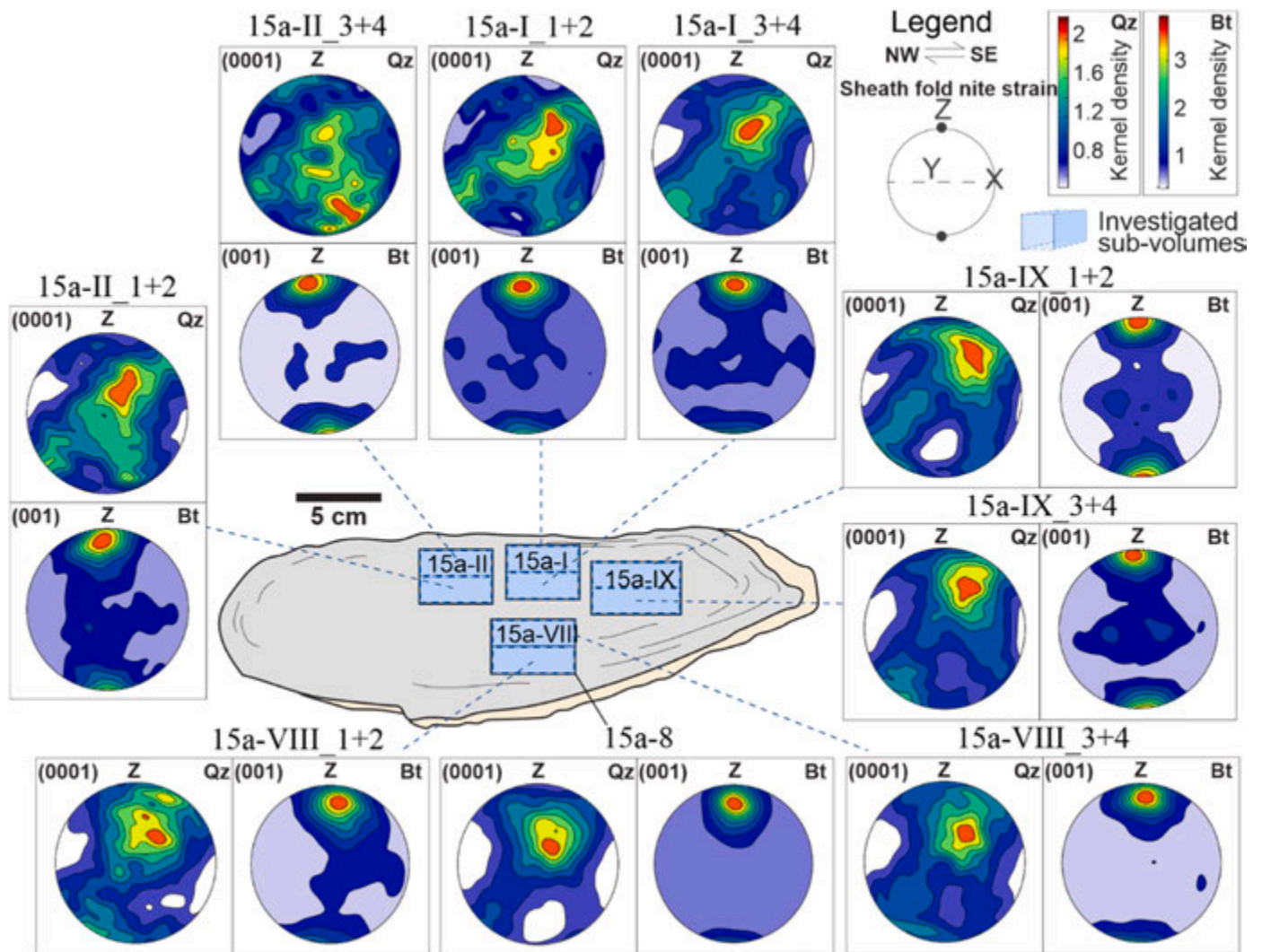
**Fig. 12.** Pole figures for quartz (Qz) and biotite (Bt) textures measured by means of ND (Neutron Diffraction) technique for the 15a slice (different investigated sub-volumes are indicated).

**Table 1**
Sample number, differential stress obtained by the subgrains and grain size method, and CPO strength highlighting J-Index and M-Index.

| Sample | N. pixels (Qz) | N. grains (Qz) | N. pixels (Bt) | N. grains (Bt) | J-Index | M-Index | Shear stress (grain size) (MPa) | Shear stress (subgrains) (MPa) |
|---|---|---|---|---|---|---|---|---|
| 15A II | 97,017 | 708 | 727 | 42 | 1.64 | 0.02 | 28.6 | 9.8 |
| 15A IV | 79,341 | 623 | 1769 | 71 | 1.72 | 0.03 | 28.3 | 8.2 |
| 15A V | 95,673 | 585 | 1122 | 55 | 1.63 | 0.02 | 27.2 | 8.3 |
| 15A IX | 109,636 | 728 | 1648 | 83 | 1.72 | 0.03 | 29.7 | 11.8 |
| 16A I | 80,150 | 694 | 3261 | 156 | 1.50 | 0.02 | 29.8 | 10.2 |
| 16A II | 90,220 | 550 | 2116 | 105 | 1.71 | 0.03 | 29.1 | 11.0 |
| 16A IV | 98,280 | 727 | 1378 | 69 | 1.64 | 0.02 | 32.5 | 8.4 |
| 17A I | 82,508 | 558 | 1788 | 78 | 1.57 | 0.02 | 25.8 | 10.0 |
| 17A II | 97,230 | 631 | 1731 | 83 | 1.81 | 0.03 | 30.2 | 9.3 |
| 17A III | 86,617 | 502 | 520 | 33 | 1.66 | 0.02 | 28.2 | 10.0 |
| 18A II | 80,995 | 540 | 2511 | 115 | 1.55 | 0.01 | 28.3 | 8.7 |
| Total volume | Qz grains 6846 | Qz pixel 997,667 | Bt grains 890 | Bt pixel 18,571 | | | | |

Table 1. Summary of the main results for quartz (Qz) and biotite (Bt). The number of pixels defining the analysed number of grains is reported. The CPO strengths, expressed by the J-Index (or "texture index", Bunge, 1982) and the M-Index (Skemer et al., 2005), are reported only for quartz. The shear stress (recalculated from the grain size, Cross et al., 2017, and the subgrains, Goddard et al., 2020, with a subgrain threshold of 1°) indicates the differential stress accommodated by quartz during dynamic recrystallization.

individual samples and for the bulk sheath fold is located in the upper-right quadrant of the projection close to the primitive circle (Fig. 10 a-d). Comparing the bulk CVA data with the CVA plots extrapolated for quartz and biotite combining all the analysed slides, we notice that the majority of the recorded strain contributing to the final plot is accommodated by quartz (Fig. 10e). Specifically, while quartz CVA is well
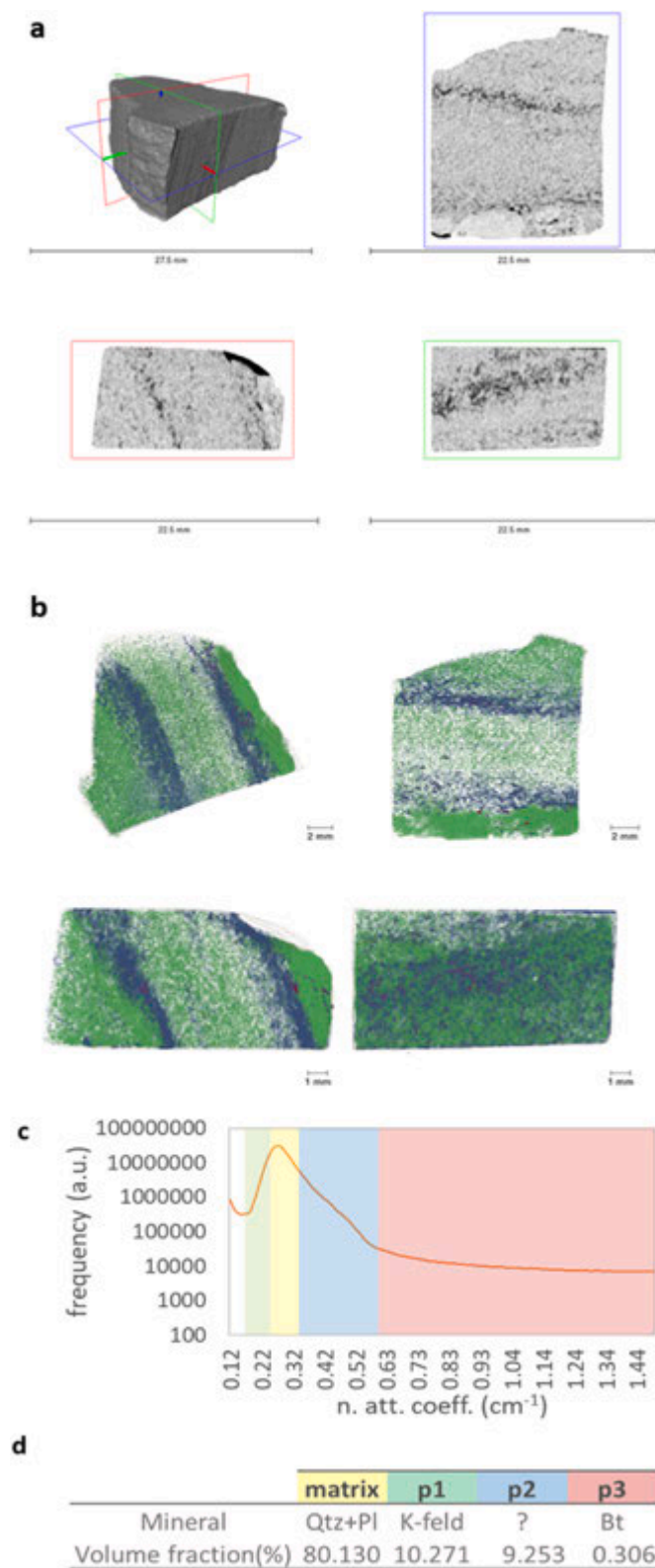
**Fig. 13.** Neutron tomography of a sub-volume (17a-V) of slice 17a (see supplementary material for volume location): (a) Orthogonal slices through the reconstructed volume of the samples with location of the cropping planes indicated in the three-dimensional model in the top-left corner (X-Z, X–Y, Y-Z planes are in red, green, and blue colour, respectively). (b) Three-dimensional distribution of mineral phases shown in different directions-one perspective and three orthogonal ones. Phases are rendered based on the colour code used to define the thresholding values adopted for the segmentation in (c) the histogram of the frequency distribution of the neutron attenuation coefficients. The phases attributed to each segmented region in the histogram and the corresponding volume fraction percentage are reported in d). (For interpretation of the references to colour in this figure legend, the reader is referred to the Web version of this article.)

(8–10 MPa) accommodated by quartz with minimal variations across the structure.

## 5. Discussion

### 5.1. CPO fabrics within sheath folds

The microstructural data suggests a minimal variation in deformation patterns within the analysed volume of the sheath fold. The main CPO findings are consistent with a top-to-SE shear sense (i.e., towards the closure of the synformal sheath) in all domains of the fold. This sense of shear is clearly detectable from pole figures of quartz c-axis patterns (Figs. 7–10), and also corroborated by ND quartz textural findings (Figs. 11 and 12), suggesting minimal flow variations developed in different structural positions within the sheath fold. Also, our CVA data indicate no significant variations of the kinematic flow (see Fig. 10). Specifically, we have shown the decoupling between the vorticity axis recorded by quartz and biotite, and how biotite CVA's plots probably reflect that the foliation was passively folded and rotated during the kinematic flow. Therefore, focusing on the quartz, that likely accommodated most of the deformation due to the kinematic flow, we can observe how, although an offset is present (see par. 5.1.4 for further considerations), the CVA distributions are well focused mostly in point maxima, with negligible variations in the direction of the vorticity vector from the inner vs outer sheath closures. In the Scandian orogenic wedge of NW Scotland, microstructural and crystal fabric indicators oriented top-to-NW are generally recorded close to thrust sheet boundaries, suggesting that either i) the rate of overthrusting was greater than the rate of transport-parallel extrusion (Holdsworth, 1989), or ii) overthrusting has outlasted and overprinted the effects of transport-parallel extrusion (see Fig. 13c of Thigpen et al., 2013). Rare top-to-ESE shear bands also reported by Lusk and Platt (2020). A quartz c-axis pattern nearly identical to the bulk deformation fabric reported here (Fig. 9a and inset of Fig. 14a) was recorded by Holdsworth and Grant (1990) for a sample collected in the proximity of the Ben Hope Thrust near the Kyle of Tongue, suggesting a comparable top-to-ESE shear sense. Similar motions, in the opposite sense to the top-to-the NW regional thrusts, have also been recently reported by Law et al. (2021) in an area south of the study area in the hanging wall of the Sgurr Beag Thrust, where both microstructures and quartz c-axis fabric indicate pervasive top down to the ESE-shearing. These authors explained these apparently conflicting observations with respect to the regional NW-directed tectonic transport as being due to reactivation of the original thrust which was overprinted by pervasive normal sense shearing of the hanging wall and footwall rocks while they remained at close to peak temperatures. Thigpen et al. (2013) also considered the possibility that the rate of transport-parallel extrusion exceeds the rate of over-thrusting, generating a net normal sense of motion along the upper surface of the thrust sheet.

There are a number of hypotheses that may be considered to help explain the mineral CPO outcomes in this study described in the following sections.

*(caption on next column)*

focused in point maxima regions and is essentially constant across the samples (Fig. 10), biotite CVAs are more inhomogeneous among the analysed volumes.

Results from subgrain piezometry (Table 1) indicate low shear stress
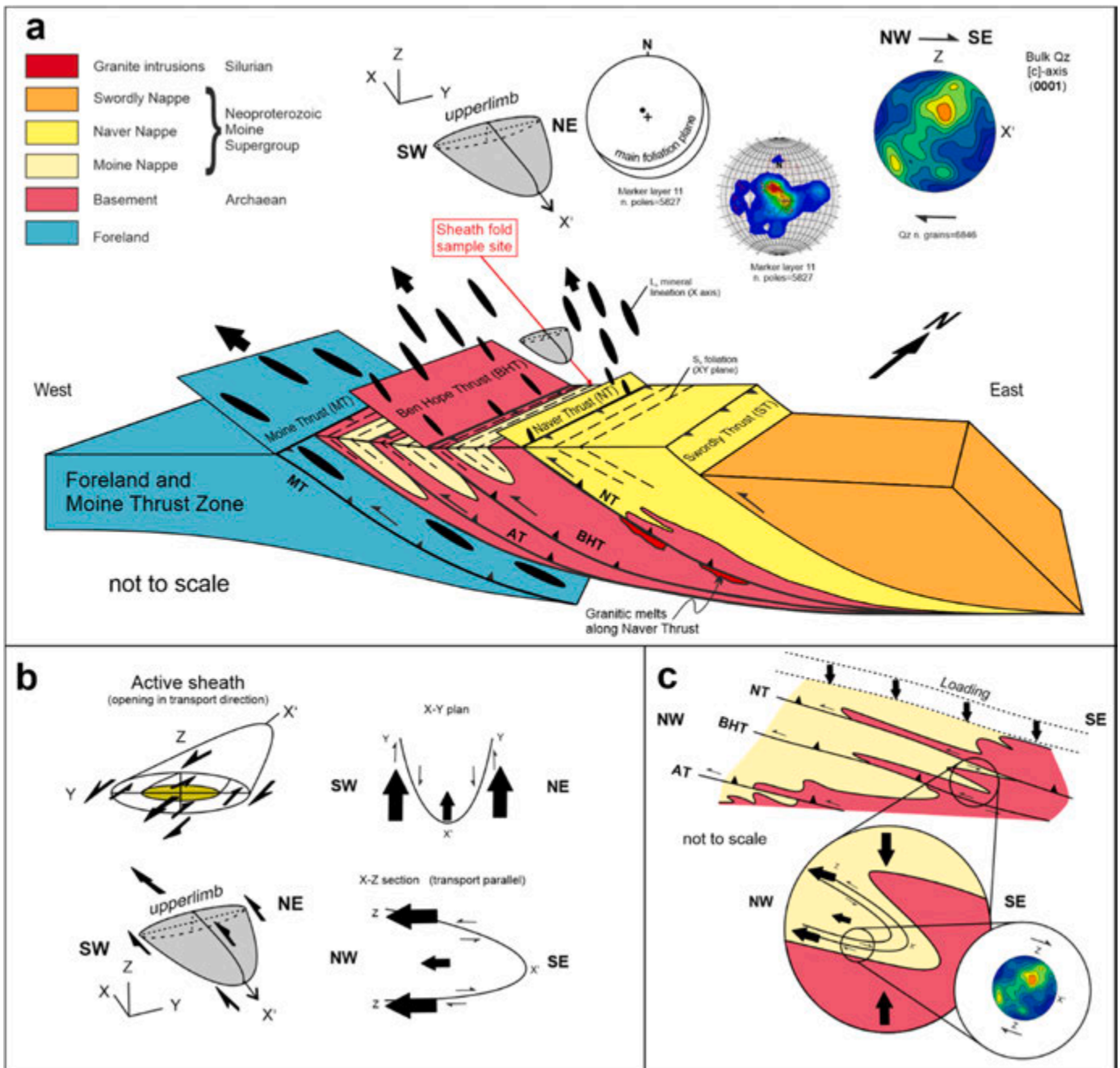
**Fig. 14.** (a) Block diagram showing the Scandian orogenic wedge of NW Scotland (not to scale) top right insets: stereoplot with poles to mylonitic foliation (Sn - marker layer 11) reconstructed by the 3D model of the sheath fold (Move software; n. 5827 surfaces were sampled) and bulk pole figure of quartz c-axes orientation (Qz grains n. 6846; fabric diagrams is viewed towards NE). (b) Mesoscopic 3D sketches of an active sheath fold (after Alsop and Holdsworth, 2012).; (c) (top) schematic diagrams of a simple ductile thrust model to explain the evolution of the Caledonian structures in the Scandian orogenic wedge (modified after Holdsworth, 1989) with lateral layer parallel extrusion and an orogenic wedge loading compatible with a sub-vertical sigma 1 and (bottom) position of the studied mesoscopic sheath fold showing a top-to-the SE shear sense in the lower hinge of a regional-scale synformal fold. Legend: AT Achness Thrust, BHT Ben Hope Thrust, NT Naver Thrust; the sheath fold is located within the Ben Hope Thrust sheet/nappe.

*5.1.1. The CPO fabric is associated with passive sheath folding*

In this model, the CPO is associated with the early formation of sheath folds and suggests passive folding with a constant sense of shear around the fold nose and across its axial surface. However, a major issue is that the CPO fabric records a top-to-SE shear direction i.e. top-to-the SE closure direction of the synformal sheath fold (Fig. 14), which is opposite to the regional (NW-directed) thrusting. The CPO fabric is therefore not in agreement with passive sheath folding created during NW-directed shear.

Furthermore, Alsop and Holdsworth's (2012) analysis of the case

study fold reveals several mesoscopic features such as lineation traces wrapping the external folded surface to form "U" shaped star-burst patterns, elliptical shapes and thickness of marker layers all consistent with an active fold opening in the (NW-directed) transport direction (Alsop and Holdsworth, 2012). In summary, the CPO fabric analysis indicates SE-directed shear and this is not consistent with passive sheath folding created during NW-directed thrusting.

*5.1.2. The CPO fabric is folded around transport-parallel hinges*

In this scenario, fold hinges that are developed parallel to transport

may fold earlier kinematic indicators including CPO fabrics. The effect of folding around transport-parallel hinges is to create an apparent reversal in shear sense, although folds in general should be used with caution to determine shear sense (e.g., Krabbendam and Leslie, 1996). In the present study, top-to-the NW shear sense preserved on the upper limb of a transport-parallel fold could therefore be folded around the hinge to create an apparent top-to-the SE shear on the lower fold limb. Within the study area, the fold hinges are generally parallel or sub-parallel to the NW-directed transport marked by the mineral lineation, resulting in the large-scale sheath folds as displayed by the Borgie Inlier that overlies the case study fold (Fig. 1b, Alsop and Holdsworth 2004). However, preservation of the top-to-the SE CPO fabrics on the lower limbs of major folds would necessitate deformation to cease almost immediately following folding so as to avoid overprinting by continued top-to-the NW thrusting. As thrusting and folding is thought to be progressive and operating across a number of ductile thrusts in the region (e.g., Alsop et al., 1996; Strachan et al., 2020), we consider it unlikely for thrusting to immediately cease following folding and therefore discount this model.

### 5.1.3. The CPO fabric post-dates the creation of the sheath fold

In this model, the CPO is related to a late phase of crystal-plastic deformation that occurred after the formation of the sheath fold and almost completely obliterated the previous fabric associated with the sheath fold phase. The CPO therefore only records the last part of the tectono-thermal evolution and may be a more realistic model since the generally low CPO intensity of the minerals found in the sheath fold could indicate a response to a late deformation phase rather than being attributable to the initial formation of the fold.

### 5.1.4. Further considerations

According to Michels et al. (2015), CVAs can be used to understand the kinematic partitioning and strain localization in poly-mineral aggregates. About kinematic partitioning, our biotite CVA data (Fig. 10), spread along small circles in the stereographic plots, are interpreted to reflect the folding and rotation of the grains during the kinematic flow. We exclude a post-kinematic recrystallization affecting such biotite as it would have been visible in the CPO plots with more scattered maxima instead of girdle distributions (e.g., Fig. 9b). Focusing on the well-defined distributions of quartz CVA (Fig. 10), we highlight that the vorticity vector recorded is located away from what one could expect in a dominant simple shear system (e.g., it is close to the primitive circle instead of at the centre of the pole figure as it should be for the type of extrusion of the thrust; see also Piette-Lauzière et al., 2020; Miranda et al., 2023 for examples). Combining such information with the quartz CPOs data and the irregular shape of the sheath fold itself (i.e. the systematic asymmetry of the sheath culminations with respect to the mineral lineation, Fig. 2a, see also Alsop and Holdsworth, 2012), we interpret our offsets as reflecting the disharmony of the main strain axes of the sheath fold with respect to the kinematic flow and possibly a post reactivation of the thrust. We highlight that also Alsop and Holdsworth (2012, their Figs. 5 and 14) recorded culmination points from adjacent folded surfaces that are systematically offset towards the SW (right when viewed down plunge from above) and this may provide a further evidence of a shear phase postdating the fold formation and affecting the CVAs.

Our estimates of P-T values inferred from OA measurements are consistent with Thigpen et al. (2013) and correspond with recent estimates by Strachan et al. (2020) who note that sheath fold geometries are locally common on all scales. Within the Moine Nappe, the widespread parallelism of hornblende with L2 in mafic rocks implies that D2 was accompanied by at least low amphibolite facies metamorphism, consistent with local occurrences of syn-to post-D2 staurolite, kyanite and sillimanite. The OA data measured in this study (Table S2), which can be attributed to the amphibolite facies condition, are therefore related to deformation developed close to peak thermal conditions.

In summary, we believe that quartz c-axis patterns of the studied sheath fold have essentially recorded one tectonic phase that has obliterated previous fabrics, such as those developed during Scandian thrusting, resulting in the development of tight-to-isoclinal F2 folds (Thigpen et al., 2013). The D2 generated a pervasive sub-horizontal foliation (S2) and a pronounced mineral stretching lineation (L2) interpreted to lie sub-parallel to the direction of Scandian thrust transport (Strachan et al., 2002, 2010; Law and Johnson, 2010 and references therein), evolving in the late stages of progressive deformation to a sheath folding phase (F3 folds). Our findings are also consistent with the model of vertical ductile thinning proposed by Thigpen et al. (2013). This model suggests a coeval component of transport-parallel extrusion of material towards the NW (i.e. the syn-orogenic topographic surface) driven by transport-parallel stretching (top-to-SE) resulting from a vertical component of pure shear shortening (orogenic wedge loading). If one considers the hypothesis of Thigpen et al. (2013) where the overthrust rate is overcome by lateral extrusion, then a later overprinting tectonic phase is not necessary to develop such a fabric.

### 5.2. Deformation patterns within sheath folds

It has long been recognized that bed-subparallel detachments may form around sheath fold closures from a km-scale (e.g., Alsop 1992, 1994; Searle and Alsop, 2007) to a metre scale (Alsop and Holdsworth, 2012). The location of detachments may be partially controlled by original lithological heterogeneity which influenced deformation in the early more 'active' stages of folding. As folding of the competent layers develops, they may locally truncate adjacent beds leading to low-angle detachments observed around sheath fold noses (e.g., Alsop, 1994; Searle and Alsop, 2007; Alsop and Holdsworth, 2012). Such folds and associated detachments are subsequently accentuated during more passive deformation associated with flow and amplification of sheath folds.

We suggest that where sheath folds comprise rheologically contrasting inter-layered units, then flexural flow may occur as a result of the differential deformation between the more competent and weaker beds (Fig. 14c). As deformation progresses, the weaker layers and interfaces undergo flexural deformation, with slip concentrating along these weaker horizons to accommodate the strain. The slip can take place parallel or oblique to the fold hinge, depending on the orientation of the stress field and the mechanical anisotropy of the rock layers. The resulting sheath folds exhibit characteristic tongue shapes, with parallel-sided limbs marked by slip along the weaker layers or interfaces. The sense of slip results in 'extrusion' of the core relative to the outer envelope of the fold, that will correspond with a top-to-the SE shear on the lower fold limb and top-to-the NW shear on the upper limb of the synform that closes to the SE (Fig. 14c).

In summary, although there is no indication of a change in CPO shear sense across the axial surface of the sheath fold that would be required by the model, the location of the sample site within a synform underlying the major Borgie sheath fold is consistent with this proposal (see Figs. 1 and 14a, c).

## 6. Conclusion

The case study fold is considered to have formed during non-coaxial deformation associated with regional NW-directed shear (Alsop and Holdsworth, 2012). The kinematics of the fold inferred from the mineral CPO are antithetic (i.e. top-to-SE) to this general NW-directed tectonic transport of large-scale folds and vergence of the main thrusts (BHT to NT). This relationship is observed in areas of high strain rate where it is not unusual to observe secondary structures showing opposite shear directions with respect to those of the main regional structure.

The sheath fold sample may therefore represent such a minor structure in which, due to a flexural flow mechanism on the inverted limb of the fold, shear senses were locally opposite to the general shear

sense that formed the main fold. Alternatively, it could reflect the local top-to-the SE-directed shear sense associated with a larger active sheath fold (Fig. 14c). However, the CPO results are not consistent with such a claim since they indicate SE-directed shear.

In view of the previous detailed morphological study of the multi-layered sheath fold by Alsop and Holdsworth (2012), together with the mineral CPO measured in the present study, we can conclude that an early active folding stage of the studied sheath fold has been extensively masked and pervasively obliterated by a top-to-SE normal shearing event. Our results suggest that even if macroscopic evidence of active folding is preserved, the earlier CPO fabric has been almost completely destroyed and it reflects instead the last deformational phases showing a constant top-to the SE sense of shear which is opposite to the main NW-directed tectonic transport of major thrusts. We note that microstructural and quartz c-axis data recently reported by Law et al. (2021) from a locality in the Caledonides of northern Scotland (e.g. Creich Peninsula in the immediate footwall and hanging wall to the Sgurr Beag thrust), also indicates a comparable normal-sense top down-SE shearing, probably developed at close to peak temperatures at ~420 Ma. We follow these authors to suggest that top-to-the SE shear may relate to the closing stages of Scandian deformation, metamorphism and cooling/exhumation.

## Author statement

Eugenio Fazio: Conceptualization, Methodology, Investigation, Writing - Original Draft, Writing - Review & Editing, Data Curation, Visualization, Supervision, Project administration, Funding acquisition; Ian G. Alsop: Conceptualization, Investigation, Resources, Writing - Review & Editing, Supervision, Project administration; Laura Nania: Conceptualization, Validation, Methodology, Investigation, Data Curation, Writing - Original Draft, Writing - Review & Editing, Visualization; Riccardo Graziani: Conceptualization, Software, Methodology, Validation, Investigation, Data Curation, Writing - Review & Editing, Visualization; Salvatore Iaccarino: Conceptualization, Investigation, Data Curation, Writing - Review & Editing; Chiara Montomoli: Conceptualization, Investigation, Writing - Review & Editing; Rodolfo Carosi: Conceptualization, Investigation, Writing - Review & Editing, Supervision; Vladimir Luzin: Conceptualization, Methodology, Software, Validation, Investigation, Resources, Data Curation, Writing - Review & Editing, Visualization, Supervision, Project administration, Funding acquisition; Floriana Salvemini: Methodology, Investigation, Resources, Data Curation, Writing - Review & Editing, Visualization; Salvatore Gambino: Methodology, Investigation, Writing - Review & Editing, Visualization; Rosolino Cirrincione: Resources, Writing - Review & Editing, Supervision; Manish A. Mamtani: Conceptualization, Investigation, Writing - Review & Editing, Supervision.

## Declaration of competing interest

The authors declare that they have no known competing financial interests or personal relationships that could have appeared to influence the work reported in this paper. The authors declare the following financial interests/personal relationships which may be considered as potential competing interests: Graziani Riccardo has patent copyright (NRCan - IPD assignment form required to develop a copyright license) licensed to His Majesty the King in Right of Canada, as represented by the Minister of Natural Resources, all rights, title and interest, including copyright and all rights under copyright. Nania Laura has patent copyright (NRCan - IPD assignment form required to develop a copyright license) licensed to His Majesty the King in Right of Canada, as represented by the Minister of Natural Resources, all rights, title and interest, including copyright and all rights under copyright.

## Data availability

Data will be made available on request.

CPO_sheath_fold_dataset (Original data) (Mendeley Data)

## Appendix A. Supplementary data

Supplementary data to this article can be found online at https://doi.org/10.1016/j.jsg.2023.105000.

## References

Aerden, D.G.A.M., Ruiz-Fuentes, A., Sayab, M., Forde, A., 2021. Kinematics of subduction in the Ibero-Armorican arc constrained by 3D microstructural analysis of garnet and pseudomorphed lawsonite porphyroblasts from Île de Groix (Variscan belt). Solid Earth 12, 971–992.

Alsop, G.I., Carreras, J., 2007. The structural evolution of sheath folds: a case study from Cap de Creus. J. Struct. Geol. 29 (12), 1915–1930.

Alsop, G.I., 1992. Progressive deformation and the rotation of contemporary fold axes in the Ballybofey Nappe, northwest Ireland. Geol. J. 27, 271–283.

Alsop, G.I., 1994. Relationships between distributed and localised shear in the tectonic evolution of a Caledonian fold and thrust zone, northwest Ireland. Geol. Mag. 131, 123–136.

Alsop, G.I., Cheer, D.A., Strachan, R.A., Krabbendam, M., Kinny, P.D., Holdsworth, R.E., Leslie, A.G., 2010. Progressive fold and fabric evolution associated with regional strain gradients: a case study from across a Scandian ductile thrust nappe, Scottish Caledonides. In: Law, R.D. (Ed.), Continental Tectonics and Mountain Building: the Legacy of Peach and Horne, vol. 335. Geological Society, London, Special Publications, pp. 253–272.

Alsop, G.I., Holdsworth, R.E., 1993. The distribution, geometry and kinematic significance of Caledonian buckle folds in the western Moine Nappe, northwestern Scotland. Geol. Mag. 130, 353–362.

Alsop, G.I., Holdsworth, R.E., 2004. The geometry and topology of natural sheath folds: a new tool for structural analysis. J. Struct. Geol. 26 (9), 1561–1589.

Alsop, G.I., Holdsworth, R.E., 2006. Sheath folds as discriminators of bulk strain type. J. Struct. Geol. 28, 1588–1606.

Alsop, G.I., Holdsworth, R.E., 2007. Flow perturbation folding in shear zones. In: Ries, A. C., Butler, R.W.H., Graham, R.D. (Eds.), Deformation of the Continental Crust: the Legacy of Mike Coward, vol. 272. Geological Society, London, Special Publications, pp. 77–103.

Alsop, G.I., Holdsworth, R.E., 2012. The three dimensional shape and localisation of deformation within multilayer sheath folds. J. Struct. Geol. 44, 110–128.

Alsop, G.I., Holdsworth, R.E., McCaffrey, K.J.W., 2007. Scale invariant sheath folds in salt, sediments and shear zones. J. Struct. Geol. 29, 1585–1604.

Alsop, G.I., Holdsworth, R.E., Strachan, R.A., 1996. Transport-parallel cross folds within a mid-crustal Caledonian thrust stack, northern Scotland. J. Struct. Geol. 18, 783–790.

Alsop, G.I., Strachan, R.A., Holdsworth, R.E., Burns, I.M., 2021. Geometry of folded and boudinaged pegmatite veins emplaced within a strike-slip shear zone: a case study from the Caledonian orogen, northern Scotland. J. Struct. Geol. 142, 104233.

Ashley, K.T., Thigpen, J.R., Law, R.D., 2015. Prograde evolution of the Scottish Caledonides and tectonic implications. Lithos 224 (225), 160–178.

Ashley, K.T., Law, R.D., Thigpen, J.R., 2017. Garnet morphology distribution in the northern part of the moine Supergroup, Scottish Caledonides. J. Metamorph. Geol. 35, 77–94.

Bons, P., Jansen, D., Mundel, F., Bauer, C.C., Binder, T., Eisen, O., et al., 2016. Converging flow and anisotropy cause large-scale folding in Greenland's ice sheet. Nat. Commun. 7, 11427.

Bunge, H.J., 1982. Texture analysis in materials science. In: Mathematical Methods, first ed. Butterworth-Heinemann, London, p. 614.

Carreras, J., Druguet, E., 2019. Complex fold patterns developed by progressive deformation. J. Struct. Geol. 125, 195–201.

Carreras, J., Druguet, E., Griera, A., 2005. Shear zone-related folds. J. Struct. Geol. 27, 1229–1251.

Carreras, J., Estrada, A., White, S., 1977. The effects of folding on the C-axis fabrics of a quartz mylonite. Tectonophysics 39, 3–24.

Cawood, T.K., Rozendaal, A., Buick, I., Frei, D., 2023. Tectonic evolution of the Aggeneys-Gamsberg ore district, South Africa, and implications for the geodynamic setting of the Namaqua sector. Ore Geol. Rev. 105440.

Cobbold, P.R., Quinquis, H., 1980. Development of sheath folds in shear regimes. J. Struct. Geol. 2, 119–126.

Crispini, L., Capponi, G., 1997. Quartz fabric and strain partitioning in sheath folds: an example from the Voltri Group (Western Alps, Italy). J. Struct. Geol. 19, 1149–1157.

Cross, A.J., Prior, D.J., Stipp, M., Kidder, S., 2017. The recrystallized grain size piezometer for quartz: an EBSD-based calibration. Geophys. Res. Lett. 44 (13), 6667–6674.

Davis, G.H., Reynolds, S.J., 1996. Structural Geology of Rocks and Regions. John Wiley & Sons.

Druguet, E., Alsop, G.I., Carreras, J., 2009. Coeval brittle and ductile structures associated with extreme deformation partitioning in a multilayer sequence. J. Struct. Geol. 31, 498–511.

Faleiros, F.M., Moraes, R., Pavan, M., Campanha, G.A.C., 2016. A new empirical calibration of the quartz c-axis fabric opening-angle deformation thermometer. Tectonophysics 671 (7), 173–182.

Fazio, E., 2019. Recognition of structures in mid-crustal shear zones and how to discern between them. In: Billi, A., Fagereng, Å. (Eds.), Problems and Solutions in Structural Geology and Tectonics. Elsevier, pp. 119–128, 2019.

Fazio, E., Ortolano, G., Visalli, R., Alsop, G.I., Cirrincione, R., Pezzino, A., 2018. Strain localization and sheath fold development during progressive deformation in a ductile shear zone: a case study of macro to microscale structures from the Aspromonte Massif, Calabria. Italian Journal of Geosciences 137 (2), 208–218.

Fazio, E., Punturo, R., Cirrincione, R., 2010. Quartz c-axis texture mapping of mylonitic metapelite with rod structures (Calabria, southern Italy): clues for hidden shear flow direction. J. Geol. Soc. India 75, 171–182.

Fazio, E., Punturo, R., Cirrincione, R., Kern, H., Pezzino, A., Wenk, H.-R., Goswami, S., Mamtani, M.A., 2017. Quartz preferred orientation in naturally deformed mylonitic rocks (Montalto shear zone–Italy): a comparison of results by different techniques, their advantages and limitations. Int. J. Earth Sci.

Feldmann, K., 1989. Texture investigations by neutron time-of-flight diffraction. Textures Microstruct. 10, 309–323.

Fiduk, J.C., Rowan, M.G., 2012. Analysis of folding and deformation within layered evaporites in Blocks BM-S-8 & -9, Santos Basin, Brazil. In: Alsop, G.I., Archer, S.G., Hartley, A.J., Grant, N.T., Hodgkinson, R. (Eds.), Salt Tectonics, Sediments and Prospectivity. Geological Society of London, 0.

Garbe, U., Randall, T., Hughes, C., Davidson, G., Pangelis, S., Kennedy, S.J., 2015. A new neutron radiography/tomography/imaging station DINGO at OPAL. Phys. Procedia 69, 27–32.

Ghosh, S.K., Hazra, S., Sengupta, S., 1999. Planar, non-planar and refolded sheath folds in the Phulad Shear Zone, Rajasthan, India. J. Struct. Geol. 21, 1715–1729.

Goddard, R.M., Hansen, L.N., Wallis, D., Stipp, M., Holyoke III, C.W., Kumamoto, K.M., Kohlstedt, D.L., 2020. A subgrain-size piezometer calibrated for EBSD. Geophys. Res. Lett. 47 (23), e2020GL090056.

Graziani, R., Larson, K.P., Law, R.D., Vanier, M.-A., Thigpen, J.R., 2021. A refined approach for quantitative kinematic vorticity number estimation using microstructures. J. Struct. Geol. 153, 104459.

Graziani, R., Larson, K.P., Soret, M., 2020. The effect of hydrous mineral content on competitive strain localization mechanisms in felsic granulites. J. Struct. Geol. 134, 104015.

Hielscher, R., Schaeben, H., 2008. A novel pole figure inversion method: specification of the MTEX algorithm. J. Appl. Crystallogr. 41, 1024–1037.

Holdsworth, R.E., 1989. The geology and structural evolution of a Caledonian fold and ductile thrust zone, Kyle of Tongue region, Sutherland, northern Scotland. J. Geol. Soc. 146, 809–823.

Holdsworth, R.E., Alsop, G.I., Strachan, R.A., 2007. Tectonic stratigraphy and structural continuity of the northernmost moine thrust zone and moine nappe, Scottish Caledonides. In: Ries, A.C., Butler, R.W.H., Graham, R.D. (Eds.), Deformation of the Continental Crust: the Legacy of Mike Coward, vol. 272. Geological Society, London, Special Publications, pp. 123–144.

Holdsworth, R.E., Grant, C.J., 1990. Convergence-related "dynamic spreading" in a mid-crustal ductile thrust zone: a possible orogenic wedge model. Geol. Soc. Spec. Publ. 54, 491–500.

Holdsworth, R.E., Strachan, R.A., Alsop, G.I., 2001. Geology of the Tongue District. Memoirs of the British Geological Survey, p. 76. Sheet 114E(Scotland).

Holdsworth, R.E., Strachan, R.A., Alsop, G.I., Grant, C.J., Wilson, R.W., 2006. Thrust sequences and the significance of low-angle, out-of-sequence faults in the northernmost moine nappe and moine thrust zone, NW Scotland. J. Geol. Soc. 163, 801–814. London.

Holdsworth, R.E., Strachan, R.A., Harris, A.L., 1994. Precambrian rocks in northern Scotland east of the moine thrust: the moine Supergroup. A revised correlation of Precambrian rocks in the British Isles 23–32.

Hudec, M.R., Jackson, M.P.A., 2007. Terra infirma: understanding salt tectonics. Earth Sci. Rev. 82, 1–28.

Hunter, N.J.R., Luzin, V., Wilson, C.J.L., 2017a. Direct measurement of the quartz c-axis using neutron diffraction. Tectonophysics 712 (713), 464–468.

Hunter, N.J.R., Weinberg, R.F., Wilson, C.J.L., Law, R.D., 2018a. A new technique for quantifying symmetry and opening angles in quartz c-axis pole figures: implications for interpreting the kinematic and thermal properties of rocks. J. Struct. Geol. 112, 1–6.

Hunter, N.J.R., Weinberg, R.F., Wilson, C.J.L., Luzin, V., Misra, S., 2018b. Microscopic anatomy of a "hot-on-cold" shear zone: insights from quartzites of the main central thrust in the Alaknanda region (Garhwal Himalaya). Bull. Geol. Soc. Am. 130, 1519–1539.

Hunter, N.J.R., Wilson, C.J.L., Luzin, V., 2017b. Comparison of quartz crystallographic preferred orientations identified with optical fabric analysis, electron backscatter and neutron diffraction techniques. J. Microsc. 265, 169–184.

Jackson, M.P.A., Vendeville, B.C., Sharp, I.R., 1994. Salt tectonics: a global perspective. AAPG Memoir 65, 51–70.

Kampmann, T.C., Stephens, M.B., Weihed, P., 2016. 3D modelling and sheath folding at the Falun pyritic Zn-Pb-Cu-(Au-Ag) sulphide deposit and implications for exploration in a 1.9 Ga ore district, Fennoscandian Shield, Sweden. Miner. Deposita 51, 665–680.

Krabbendam, M., Leslie, A.G., 1996. Folds with vergence opposite to the sense of shear. J. Struct. Geol. 18, 777–781.

Kruhl, J.H., 1996. Prism- and basal-plane parallel subgrain boundaries in quartz: a microstructural geothermobarometer. J. Metamorph. Geol. 14, 581–589.

Law, R.D., 2014. Deformation thermometry based on quartz c-axis fabrics and recrystallization microstructures: a review. J. Struct. Geol. 66, 129–161.

Law, R.D., Johnson, M.R.W., 2010. Microstructures and crystal fabrics of the Moine Thrust zone and Moine Nappe: History of research and changing tectonic interpretations. Geol. Soc. Spec. Pub. 335, 443–503. https://doi.org/10.1144/SP335.21.

Law, R.D., Thigpen, J.R., Mazza, S.E., Mako, C.A., Krabbendam, M., Spencer, B.M., Ashley, K.T., Strachan, R.A., Davis, E.F., 2021. Tectonic transport directions, shear senses and deformation temperatures indicated by quartz c-Axis fabrics and microstructures in a NW-SE transect across the moine and Sgurr Beag thrust sheets, Caledonian orogen of northern Scotland. Geosciences 11.

Lusk, A.D., Platt, J.P., 2020. The deep structure and rheology of a plate boundary-scale shear zone: Constraints from an exhumed Caledonian shear zone, NW Scotland. Lithosphere 2020, 8824736.

Mako, C.A., Law, R.D., Caddick, M.J., Thigpen, J.R., Ashley, K.T., Cottle, J., Kylander-Clark, A., 2019. Thermal evolution of the Scandian hinterland, Naver nappe, northern Scotland. Geological Society of London Journal 176, 669–688.

Mako, C.A., Caddick, M.J., Law, R.D., Thigpen, J.R., 2023. Monazite-xenotime thermometry: a review of best practices and an example from the Caledonides of Northern Scotland. In: Schijnel, et al. (Eds.), Minor Minerals, Major Implications: Using Key Mineral Phases to Unravel the Formation and Evolution of Earth's Crust, vol. 537. Geological Society of London, Special Publication.

Maino, M., Adamuszek, M., Schenker, F.L., Seno, S., Dabrowski, M., 2021. Sheath fold development around deformable basement inclusions: integration of field-analysis (Cima Lunga unit, Central Alps) and 3D numerical models. J. Struct. Geol. 144, 104255.

Merschat, A.J., Hatcher Jr., R.D., Davis, T.L., 2005. The northern Inner Piedmont, southern Appalachians, USA: kinematics of transpression and SW-directed mid-crustal flow. J. Struct. Geol. 27 (7), 1252–1281.

Michels, Z.D., Kruckenberg, S.C., Davis, J.R., Tikoff, B., 2015. Determining vorticity axes from grain-scale dispersion of crystallographic orientations. Geology 43, 803–806.

Micieli, D., Minniti, T., Gorini, G., 2019. NeuTomPy toolbox, a Python package for tomographic data processing and reconstruction. SoftwareX 9, 260–264.

Minnigh, L.D., 1979. Structural analysis of sheath folds in a meta-chert from the western Italian Alps. J. Struct. Geol. 1, 275–282.

Miranda, E.A., Brown, V., Schwartz, J.J., Klepeis, K.A., 2023. Making sense of shear zone fabrics that record multiple episodes of deformation: electron backscatter diffraction–derived and crystallographic vorticity axis–enhanced petrochronology. Geology 51, 591–596.

Morales, L.F.G., Casey, M., Lloyd, G.E., Williams, D.M., 2011a. Kinematic and temporal relationships between parallel fold hinge lines and stretching lineations: a microstructural and crystallographic preferred orientation approach. Tectonophysics 503, 207–221.

Morales, L.F.G., Mainprice, D., Lloyd, G.E., Law, R.D., 2011b. Crystal fabric development and slip systems in a quartz mylonite: an approach via transmission electron microscopy and viscoplastic self-consistent modelling. Geol. Soc. Spec. Publ.

Morgan, S.S., Law, R.D., 2004. Unusual transition in quartzite dislocation creep regimes and crystal slip systems in the aureole of the Eureka Valley–Joshua Flat–Beer Creek plúton, California: a case for anhydrous conditions created by decarbonation reactions. Tectonophysics 384, 209–231.

Mudruk, S.V., Balagansky, V.V., Raevsky, A.B., Rundkvist, O.V., Matyushkin, A.V., Gorbunov, I.A., 2022. Complex shape of the Palaeoproterozoic Serpovidny refolded mega-sheath fold in northern Fennoscandia revealed by magnetic and structural data. J. Struct. Geol. 154, 104492.

Nania, L., Montomoli, C., Iaccarino, S., Leiss, B., Carosi, R., 2022. Multi-stage evolution of the south Tibetan detachment system in central Himalaya: insights from carbonate-bearing rocks. J. Struct. Geol. 158, 104574.

Neumann, B., 2000. Texture development of recrystallised quartz polycrystals unravelled by orientation and misorientation characteristics. J. Struct. Geol. 22 (11–12), 1695–1711.

Oriolo, S., Schulz, B., Hueck, M., Oyhantçabal, P., Heidelbach, F., Sosa, G., van den Kerkhof, A., Wemmer, K., Fossen, H., Druguet, E., Walter, J., Cavalcante, C., Siegesmund, S., 2022. The petrologic and petrochronologic record of progressive vs polyphase deformation: opening the analytical toolbox. Earth Sci. Rev. 234.

Ortolano, G., Fazio, E., Visalli, R., Alsop, G.I., Pagano, M., Cirrincione, R., 2020. Quantitative microstructural analysis of mylonites formed during Alpine tectonics in the western Mediterranean realm. J. Struct. Geol. 131.

Park, A.F., 1988. Geometry of sheath folds and related fabrics at the Luikonlahti mine, Svecokarelides, eastern Finland. J. Struct. Geol. 10 (5), 487–498.

Passchier, C.W., Trouw, R.A.J., 2005. Microtectonics. Springer Science & Business Media.

Pérez-Valera, F., Sánchez-Gómez, M., Pérez-López, A., Pérez-Valera, L.A., 2017. An evaporite-bearingaccretionary complex in the northernfront of the Betic-Rif orogen. Tectonics 36, 1006–1036.

Piette-Lauzière, N., Larson, K.P., Kellett, D.A., Graziani, R., 2020. Intracrystalline vorticity record of flow kinematics during shear zone reactivation. J. Struct. Geol. 140, 104104.

Punturo, R., Mamtani, M.A., Fazio, E., Occhipinti, R., Renjith, A.R., Cirrincione, R., 2017. Seismic and magnetic susceptibility anisotropy of middle-lower continental crust: insights for their potential relationship from a study of intrusive rocks from the Serre Massif (Calabria, southern Italy). Tectonophysics 712 (713), 542–556.

Quinquis, H., Audren, C., Brun, J.P., Cobbold, P., 1978. Intensive progressive shear in Ile de Groix blueschists and compatibility with subduction or obduction. Nature 274, 43–45.

Ramsay, J.G., 1967. Folding and Fracturing of Rocks. McGraw-Hill, New York.

Ramsay, J.G., Huber, M.I., 1987. "The techniques of modern structural geology. In: Folds and Fractures.", vol. 2. Academic Press, London.

Ramsay, J.G., 1980. Shear zone geometry: a review. J. Struct. Geol. 2, 83–99.

Ramsay, J.G., Huber, M.I., 1983. The Techniques of Modern Structural Geology, ume 1. Strain analysis" Academic Press, London.

Reber, J.E., Dabrowski, M., Galland, O., Schmid, D.W., 2013a. Sheath fold morphology in simple shear. J. Struct. Geol. 53, 15–26.

Reber, J.E., Dabrowski, M., Schmid, D.W., 2012. Sheath fold formation around slip surfaces. Terra. Nova 24.

Reber, J.E., Galland, O., Cobbold, P.R., Veslud, C.L.C. de, 2013b. Experimental study of sheath fold development around a weak inclusion in a mechanically layered matrix. Tectonophysics 586, 130–144.

Reddy, G.P.O., 2018. Digital image processing: principles and applications. In: Reddy, G., Singh, S. (Eds.), Geospatial Technologies in Land Resources Mapping, Monitoring and Management, Geotechnologies and the Environment, vol. 21. Springer, Cham.

Renjith, A.R., Mamtani, M.A., Urai, J.L., 2016. Fabric analysis of quartzites with negative magnetic susceptibility – does AMS provide information of SPO or CPO of quartz? J. Struct. Geol. 82, 48–59.

Roberts, R.G., 1987. Ore deposit models# 11. Archean lode gold deposits. Geosci. Can. 14 (1), 37–52.

Rosas, F., Marques, F.O., Luz, A., Coelho, S., 2002. Sheath folds formed by drag induced by rotation of rigid inclusions in viscous simple shear flow: nature and experiment. J. Struct. Geol. 24, 45–55.

Rowan, M.G., Vendeville, B.C., 2006. Foldbelts with early salt withdrawal and diapirism: physical model and examples from the northern Gulf of Mexico and the Flinders Ranges, Australia. Mar. Petrol. Geol. 23, 871–891.

Rozendaal, A., Rudnick, T.K., Heyn, R., 2017. Mesoproterozoic base metal sulphide deposits in the Namaqua sector of the Namaqua-Natal Metamorphic Province, South Africa: a review. S. Afr. J. Geol. 120, 153–186.

Schaeben, H., 1997. A simple standard orientation density function: the hyperspherical de la Vall'ee Poussin kernel. Phys. Status Solidi 200, 367–376.

Schmid, S.M., Casey, M., 1986. Complete fabric analysis of some commonly observed quartz c-axis patterns. Mineral and Rock Deformation: Laboratory Studies 36, 263–286.

Schulz, B., Steenken, A., Siegesmund, S., 2008. Geodynamic evolution of an Alpine terrane—the Austroalpine basement to the south of the Tauern window as a part of the Adriatic Plate (eastern Alps). Geological Society, London, Special Publications 298 (1), 5–44.

Searle, M.P., Alsop, G.I., 2007. Eye to eye with a mega-sheath fold: case study from Wadi Mayh, northern Oman Mountains. Geology 35, 1043–1046.

Shelley, D., Bossière, G., 1999. Ile de Groix: retrogression and structural development in an extensional regime. J. Struct. Geol. 21, 1441–1455.

Skemer, P., Katayama, I., Jiang, Z., Karato, S.I., 2005. The misorientation index: development of a new method for calculating the strength of lattice-preferred orientation. Tectonophysics 411, 157–167.

Southern, S.C., Mosher, S., Orlandini, O.F., 2022. Strain partitioning in the moine nappe, northernmost Scotland. Geosphere 19 (1), 47–74.

Stipp, M., Stünitz, H., Heilbronner, R., Schmid, S.M., 2002. The eastern Tonale fault zone: a 'natural laboratory' for crystal plastic deformation of quartz over a temperature range from 250 to 700 °C. J. Struct. Geol. 24 (Issue 12), 1861–1884.

Strachan, R.A., Smith, M., Harris, A.L., Fettes, D.J., Trewin, N.H., 2002. The Geology of Scotland. Geological Society, London.

Strachan, R.A., Alsop, G.I., Ramezani, J., Frazer, R.E., Burns, I., Holdsworth, R.E., 2020. Patterns of Silurian deformation and magmatism during sinistral oblique convergence, northern Scottish Caledonides. J. Geol. Soc. 177, 893–910.

Strachan, R.A., Holdsworth, R.E., Krabbendam, M., Alsop, G.I., 2010. The Moine Supergroup of NW Scotland: insights into the analysis of polyorogenic supracrustal sequences. In: Law, R.D., Butler, R.W.H., Holdsworth, R.E., Krabbendam, M., Strachan, R.A. (Eds.), Continental Tectonics and Mountain Building: the Legacy of Peach and Horne, vol. 335. Geological Society, London, Special Publications, pp. 231–252.

Stünitz, H., 1991. Folding and shear deformation in quartzites, inferred from crystallographic preferred orientation and shape fabrics. J. Struct. Geol. 13, 71–86.

Thigpen, J.R., Law, R.D., Loehn, C.L., Strachan, R.A., Tracy, R.J., Lloyd, G.E., Roth, B.L., Brown, S.J., 2013. Thermal structure and tectonic evolution of the Scandian orogenic wedge, Scottish Caledonides: integrating geothermometry, deformation temperatures and conceptual kinematic-thermal models. J. Metamorph. Geol. 31, 813–842.

Thigpen, J.R., Ashley, K.T., Mako, C., Law, R.D., Spencer, B., 2021. Interplay between crustal-scale thrusting, high metamorphic heating rates and the development of inverted thermal metamorphic gradients: numerical models and examples from the Caledonides of northern Scotland. Tectonics 40, e2021TC006716.

Toy, V.G., Prior, D.J., Norris, R.J., 2008. Quartz fabrics in the Alpine Fault mylonites: influence of pre-existing preferred orientations on fabric development during progressive uplift. J. Struct. Geol. 30, 602–621.

Vogel, S.C., Priesmeyer, H.-G., 2006. 2. Neutron production, neutron facilities and neutron instrumentation. In: Wenk, H.R. (Ed.), Neutron Scattering in Earth Sciences. De Gruyter, Berlin, Boston, pp. 27–58.

Wheeler, J., Prior, D.J., Jiang, Z., Spiess, R., Trimby, P.W., 2001. The petrological significance of misorientations between grains. Contrib. Mineral. Petrol. 141 (1), 109.

White, S.H., 2010. Mylonites: lessons from eriboll. In: Law, R.D., Butler, R.W.H., Holdsworth, R.E., Krabbendam, M., Strachan, R.A. (Eds.), Continental Tectonics and Mountain Building, the Legacy of Peach and Horne, 335, 2010. Geological Society, London, Special Publication, pp. 505–542.

Wilson, C.J.L., Hunter, N.J.R., Luzin, V., 2022. Crystallographic preferred orientation of quartz deformed at granulite conditions: the Kalinjala shear zone, port Neill, south Australia. Aust. J. Earth Sci. 69 (8), 1119–1131.